

A Bayesian multiscale CNN framework to predict local stress fields in structures with microscale features

Vasilis Krokos^{1,2,*}, Viet Bui Xuan², Stéphane P. A. Bordas³, Philippe Young⁴, and Pierre Kerfriden^{5,1,*}

¹*Cardiff School of Engineering, Cardiff University, UK*

²*Synopsys Northern Europe Ltd, Exeter, UK*

³*Institute for Computational Engineering, Faculty of Science, Technology and Communication, University of Luxembourg, Luxembourg*

⁴*School of Engineering, Mathematics and Physical Sciences, University of Exeter, Exeter, UK*

⁵*Centre des Matériaux, Mines ParisTech, Evry, France*

* *Corresponding authors: Vasilis Krokos, KrokosV@cardiff.ac.uk; Pierre Kerfriden, pierre.kerfriden@mines-paristech.fr*

April 5, 2021

Abstract

The purpose of this work is to train an Encoder-Decoder Convolutional Neural Networks (CNN) to automatically add local fine-scale stress corrections to coarse stress predictions around unresolved microscale features. We investigate to what extent such a framework provides reliable stress predictions inside and outside particular training sets. Incidentally, we aim to develop efficient offline data generation methods to maximise the domain of validity of the CNN predictions. To achieve these ambitious goals, we will deploy a Bayesian approach providing not point estimates, but credible intervals of the fine-scale stress field to evaluate the uncertainty of the predictions. This will automatically encompass the lack of knowledge due to unseen macro and micro features. The uncertainty will be used in a Selective Learning framework to reduce the data requirements of the network. In this work we will investigate stress prediction in 2D porous structures with randomly distributed circular holes.

Keywords: CNN, Multi-scale, Probabilistic inference, Surrogate modeling

1 Introduction

Multi-scale structures are very common in industrial and bio-mechanical applications, for instance composite materials and trabecular bones. Full Finite Element Analysis (FEA) for stress prediction is usually very expensive in these structures as the FE mesh needs to be very dense to capture the effect of the fine scale features. Therefore, a common approach is to use a coarse scale mesh to predict the global stress field and to perform local scale corrections in the areas where the fine scale features are present.

The effect of fine (micro) scale features on the global (macro) stress field can be expressed using Stress Intensity Factors (SIFs). SIFs can be calculated analytically but only for spherical or elliptical isolated micro scale features, or specific assemblies of such features where the main axis of inertia is aligned with the principal stress on semi-finite or infinite planes [Pilkey and Pilkey, 2008]. Additionally,

analytical SIFs assume a separation of scales and thus require the application of homogeneous boundary conditions at infinity.

In this work we will use a non-parametric regression model to perform the local corrections. We do not want to explicitly parameterise the micro and macro scale geometric features nor assume scale separability. A promising approach that satisfies all these constraints is a Convolutional Neural Network (CNN). A CNN is a specific type of Neural Network (NN) designed to work with images. CNNs have been vastly used for tasks like classification, localisation and segmentation and are able to recognise arbitrary shapes and textures as long as these are relevant to their objective [Wu et al., 2015; Zhang et al., 2018; Aladem and Rawashdeh, 2020]. Therefore, our approach is not a priori limited to any particular statistics of the geometric features but in practice we have to stay close to the ones represented in the training set. Additionally, we can use the full macro scale stress fields as input to the CNN, not only hand-crafted averages such as the ones used in homogenisation theory [Sanchez-Palencia, 1986]. Consequently, we can assume scale separability and apply arbitrary boundary conditions at infinity. Lastly, real medical or industrial data are hard to find and often expensive, so we aim to train our CNN on simpler, artificial, datasets and find a way to transfer our knowledge to real cases. To achieve that we are going to train our CNN using only patches of the geometry, so the CNN will be completely agnostic to the overall structure and will learn to identify the effect of microscale features on the macro stress field. An overview of the method can be seen in [Fig 1].

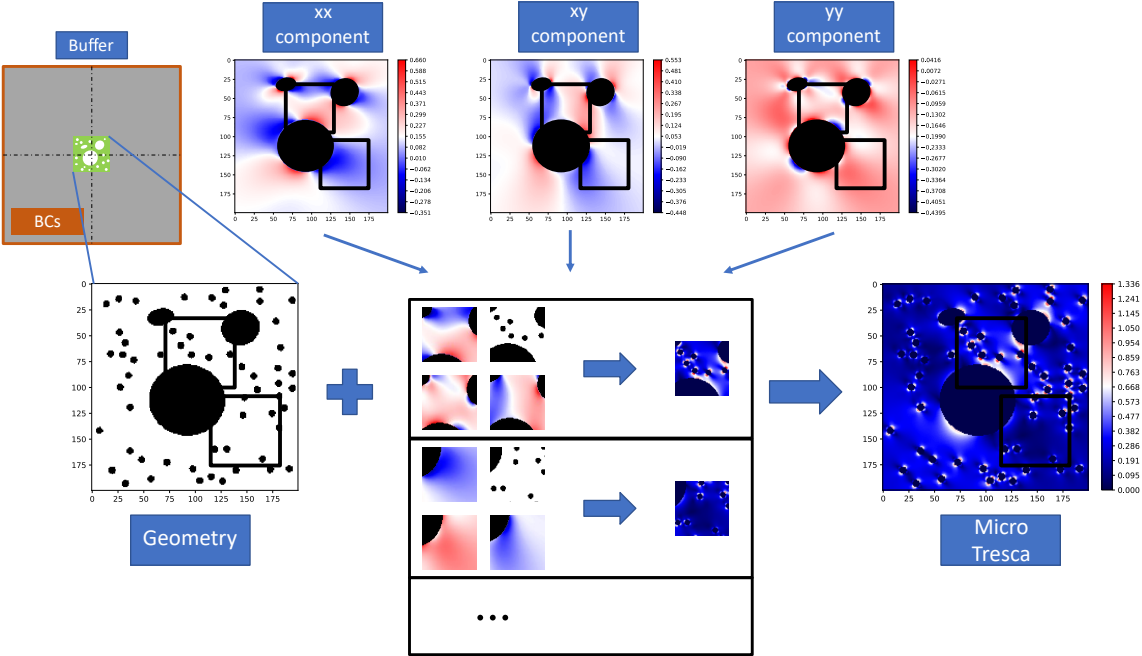


Figure 1: The multifidelity approach to stress predictions as it is pursued in this article. The inputs are the components of the macro scale stress tensor to the top and the micro scale geometry to the left. In the bottom middle image we can see that we operate on patches of the structure and calculate the output - here the micro Tresca stress - at the patch level. Lastly, on the right hand-side we can see the micro Tresca stress on the entire image, this image is reconstructed from the patches. Our model takes as input low fidelity data (macro scale stress components), and produces high fidelity data (micro scale Tresca).

Although Neural Networks (NNs) are nowadays used in a wide range of applications they usually lack one very important feature. The vast majority of NNs fail to incorporate uncertainty information in their predictions. That makes them overconfident when facing data far away from the training set, something that can lead to harmful consequences for critical tasks. Even worse, in classification tasks,

predictive probabilities obtained after the softmax layer are often erroneously interpreted as model confidence when in reality a NN can be very uncertain even with a very high softmax output [Gal and Ghahramani, 2016].

NNs that can provide uncertainty information are called Bayesian Neural Networks (BNNs). The extracted uncertainty from a BNN is expected to increase far from the dataset or in high noise areas warning us not to trust the prediction. On the other hand low uncertainty implies that the BNN is confident to make a prediction for the specific input and thus the prediction is sensible. There are 2 common ways to quantify the uncertainty in a NN and get a probabilistic output. The first one is the Bayes by Backprop method [Blundell et al., 2015]. This is a proper Bayesian treatment of the model where the parameters of the network are replaced by distributions, often but not necessarily Gaussians. The second option is by using dropout as Bayesian approximation [Gal and Ghahramani, 2016]. This method does not require changes in the architecture of the NN and the main idea is to use the dropout even during inference to introduce randomness into the network.

Although the uncertainty in itself is a very important property, BNNs are also employed to solve another, challenging problem with modern NNs, namely the lack of labelled data. Modern Deep Neural Networks (DNNs) are extremely data hungry, but labelled data are usually hard to find and expensive either in terms of time or money. This is true in our case as well. To reduce the labelled data requirements we will employ a Selective Learning (SL) framework that will help us identify the data that contain new, useful information and label only these. Selective learning with image data is a challenging task with a very sparse existing literature [Holub et al., 2008; Joshi et al., 2009; Li and Guo, 2013; Gal and Ghahramani, 2016; Gal et al., 2017].

Machine Learning (ML) has already been used in fields such as solid mechanics and bio mechanics. One of the earliest works of using ML models as surrogates for FEA is from [Liang et al., 2018] who developed an image-image deep learning framework to predict the aortic wall stress distribution where the mechanical behaviour in the FEA model was described by a fibre-reinforced hyperelastic material model. Other NNs with fully connected layers have then been used for stress predictions for non-linear materials but simple beam structures as shown by [Roewer-Despres et al., 2018; Meister et al., 2018]. Later, [Mendizabal et al., 2019] used a CNN for the prediction of nonlinear soft tissue deformation on more complicated structures such as a liver but without any kind of microscale features. Moreover, [Nie et al., 2019] deployed a CNN model for stress prediction on simple structures with geometric features but not on multi-scale problems as the size of these features was comparable to the size of the structure. Also, [Jiang et al., 2020] used a GAN to analyze mechanical stress distributions on a set of structures encoded as high and low resolution images. A variety of loading and boundary conditions has been used and some of them resembled the effect of isolated microstructural features. Recently, [Sun et al., 2020] based on the architecture of [Nie et al., 2019] created an Encoder-Decoder CNN for the prediction of stress field on Fiber-reinforced Polymers but their samples come from a single specimen and with a single FE simulation implying low generalisation ability both in terms of different structures and loading/boundary conditions. Additionally, they predict only the z component of the stress tensor and they report a value of about 70% in their evaluation metric. Lastly, [Wang et al., 2020] used a Convolutional Aided Bidirectional Long Short-term Memory Network to predict the sequence of maximum internal stress until material failure.

In contrast to all the aforementioned approaches our model is able to make predictions in multiscale cases, where multiple microscale features are interacting with each other and the macroscale structure. Also, our NN is trained on patches of different structures under different boundary conditions thus it can be applied to a much broader set of macro scale features and loadings. Furthermore, because we use the cheap macroscale stress as input, the NN only needs to learn how the microscale features are affecting the macro scale stress; further contributing to having a model that generalizes well in unseen cases. Moreover, we managed to incorporate uncertainty information into our prediction allowing us to make confident predictions or be aware of the potentially large error in the prediction. Lastly, we proposed a SL framework to tackle the well known problem of scarcity of labelled data.

2 Methods and Governing Equations

In this section we will discuss the reference multiscale mechanical model that we aim to solve online using the trained CNN and we will also introduce definitions and notations that will be necessary for us to explain our methodology.

2.1 General problem of elasticity

We consider a 2D body occupying domain $\Omega \in \mathbb{R}^2$ with a boundary $\partial\Omega$. The body is subjected to prescribed displacements U_D on its boundary $\partial\Omega_u$ and prescribed tractions T_D on the complementary boundary $\partial\Omega_T = \partial\Omega \setminus \partial\Omega_u$. The equations of linear elasticity under the plane strain assumption are as follows [Eq. 1a - 1d].

$$-\nabla \cdot \boldsymbol{\sigma} = \mathbf{f} \text{ in } \Omega \quad (1a)$$

$$\boldsymbol{\sigma} \cdot \mathbf{n} = T_D \text{ on } \partial\Omega_T \quad (1b)$$

$$\boldsymbol{\sigma} = \lambda \text{tr}(\boldsymbol{\epsilon})I + 2\mu\boldsymbol{\epsilon} \quad (1c)$$

$$\boldsymbol{\epsilon} = \frac{1}{2}(\nabla\mathbf{u} + (\nabla\mathbf{u})^\top) \quad (1d)$$

where $\boldsymbol{\sigma}$ is the stress tensor, \mathbf{f} is the body force per unit volume, λ and μ are Lamé elasticity parameters for the material in Ω , I is the identity tensor, tr is the trace operator on a tensor, $\boldsymbol{\epsilon}$ is the symmetric strain-rate tensor (symmetric gradient), \mathbf{u} is the displacement vector field and lastly \mathbf{n} is the outward unit normal to Ω .

We are interested in predicting the stress field and more specifically a fracture indicator. A proper fracture indicator is the Tresca stress. The Tresca stress can be calculated given the stress tensor as described below: The stress tensor can be rotated mechanically [Eq. 2] using the rotation matrix [Eq. 3]. The resulted components of the stress tensor after the rotation can be found in [Eq. 4a - 4c]. From [Eq. 4c] we can conclude that there must be an angle θ_p such that the shear stress after rotation is zero [Eq. 5]. After inserting θ_p into [Eq. 4a, 4b] we can calculate the 2 principal stress components [Eq. 6]. Tresca stress is equal to $\frac{1}{2}(\sigma_{\max} - \sigma_{\min})$.

$$\boldsymbol{\sigma}' = Q \cdot \boldsymbol{\sigma} \cdot Q^\top \quad (2)$$

$$Q = \begin{bmatrix} \cos(\theta) & -\sin(\theta) \\ \sin(\theta) & \cos(\theta) \end{bmatrix} \quad (3)$$

$$\sigma'_{xx} = \sigma_{xx} \cos^2 \theta + \sigma_{yy} \sin^2 \theta + 2\tau_{xy} \sin \theta \cos \theta \quad (4a)$$

$$\sigma'_{yy} = \sigma_{xx} \sin^2 \theta + \sigma_{yy} \cos^2 \theta - 2\tau_{xy} \sin \theta \cos \theta \quad (4b)$$

$$\tau'_{xy} = (\sigma_{yy} - \sigma_{xx}) \sin \theta \cos \theta + \tau_{xy}(\cos^2 \theta - \sin^2 \theta) \quad (4c)$$

$$\tan(2\theta_P) = \frac{2\tau_{xy}}{\sigma_{xx} - \sigma_{yy}} \quad (5)$$

$$\sigma_{\max}, \sigma_{\min} = \frac{\sigma_{xx} + \sigma_{yy}}{2} \pm \sqrt{\left(\frac{\sigma_{xx} - \sigma_{yy}}{2}\right)^2 + \tau_{xy}^2} \quad (6)$$

2.2 Multiscale Problem

Assuming a structure with both macroscale and microscale features like the one in [Fig 2] we assume that elasticity can be written over $\bar{\Omega}$, where microscale features are ignored or averaged, through a modification of the constitutive law (i.e. standard homogenisation) as for example in [Sanchez-Palencia, 1986]. We assume that the macro stress prediction along with the microscale information in an domain surrounding a Region Of Interest (ROI) are sufficient to predict the micro stress field in the ROI up to an acceptable level of accuracy. This assumption is backed up by Saint-Venant’s principle, stating that the micro effect in a subregion $B \subset \bar{\Omega}$ can be fully predicted knowing the macroscopic solution, if we look sufficiently far away from the boundaries of B as shown in [Fig 2].

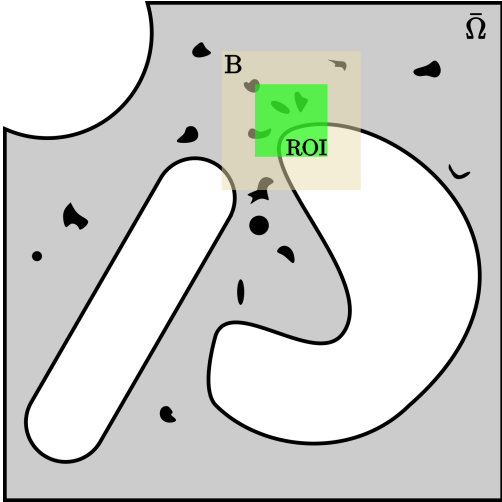


Figure 2: Sketch of a multiscale geometry. With gray the domain $\bar{\Omega}$. Two macroscale features are visible and black areas correspond to microscale features. In brown, we see a subregion B where the macro stress field and the microscale information are available and with green the ROI where the micro Tresca can be calculated.

In our case we assume a homogeneous distribution of spherical pores as microscale features. Nevertheless our surrogate model is completely agnostic to the shape of the geometric features and this information is only available through the training examples.

2.3 Input-output strategy

One strategy is to work on the entire domain as described in [Zhang et al., 2020; Sasaki and Igarashi, 2019] for topology optimisation. Unfortunately, in our problem this strategy suffers from high computational requirements both in terms of training the NN and in creating enough data to train on. Most importantly it will result in poor generalization as the NN will unavoidably try to learn the specific macrostructures present in the dataset.

Another, better suited, strategy for our case is first to solve for the stress in the whole domain and then to divide the domain in squares that we call patches as can be seen in [Fig 3]. Therefore, we can consider each patch as a training example (instead of each domain). This strategy will reduce the computational requirements because we can extract many patches from a single domain and also the NN will have inputs of smaller size. Last but not least, this strategy will result in better generalization because the NN is encouraged to learn how the microstructural features are affecting the global stress field instead of learning the specific structures present in the training dataset.

As already discussed, according to Saint-Venant’s principle we cannot fully predict the micro stress in the patch but only in a ROI far from the boundaries. Consequently, we need to provide all the available information in the patch to the NN (macro stress field and microscale features) but we can only make a micro stress prediction in the ROI. Specifically, the input of our model will be the full macro stress tensor in the patch along with the microscale features while the output will be the Tresca stress in the ROI.

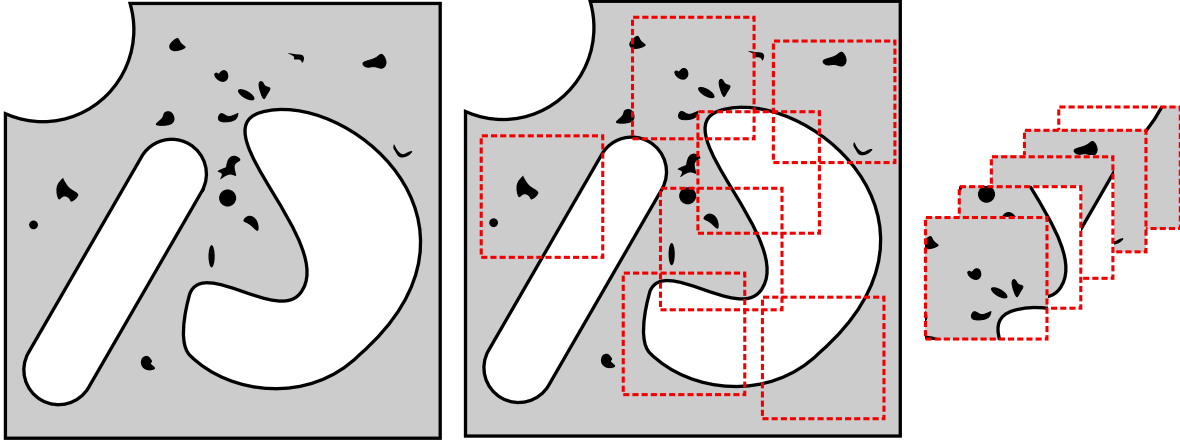


Figure 3: On the left the original structure that we want to analyze. In the middle we randomly choose 7 patches that correspond to the red squares. On the right some of the patches that we will feed to the NN.

2.4 Training dataset

For the purpose of training our model we have assumed a distribution of elliptical pores as macroscale features. We consider all the microscale features as circles with the same radius, R . We assume that for a distance larger than 4 radii from the center of the microscale features the micro effect on the global stress field is negligible, for instance in the case of an infinite plate under uni-axial loading the max stress at $r = 4R$ is 1.04 times the macro stress [Pilkey and Pilkey, 2008]. Based on that the micro feature length is $2R$, and the interaction length is equal to $3R$. Given those 2 parameters we conclude that the patch length should be $18R$ and the ROI should be a $[8R \times 8R]$ window in the middle of the patch as shown in [Fig 4].

The boundary conditions are applied to a buffer area where the mesh is much coarser, as can be seen in [Fig 5]. The buffer area allows us to apply boundary conditions without introducing boundary effects on the fine mesh area. Additionally, because the mesh in the buffer area is very coarse the computational cost remains practically the same. We apply displacement as boundary conditions [Eq. 7].

$$u = \begin{bmatrix} E_{xx} & E_{xy} \\ E_{xy} & E_{yy} \end{bmatrix} (X - X_0)^\top \quad (7)$$

where E_{xx} is the far field displacement along the x direction, E_{xy} is the far field displacement along the xy direction, E_{yy} is the far field displacement along the y direction, X is the position of a point in \mathbb{R}^2 and X_0 is the initial position of the center of the body in \mathbb{R}^2 .

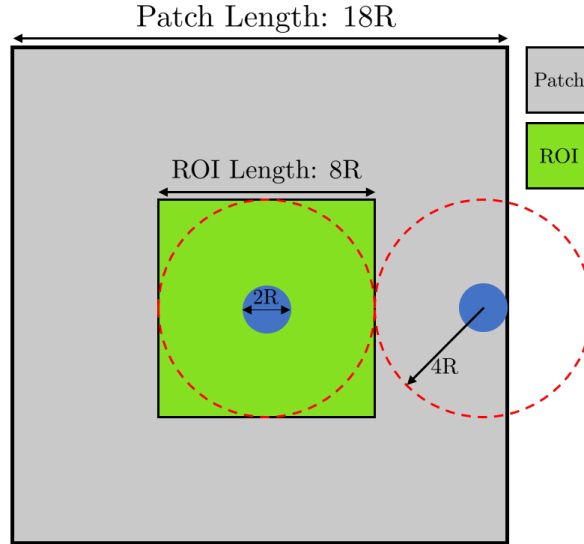


Figure 4: A sketch of the patch. In grey we see the patch, in green the region of interest and with the blue we can see circles of radius equal to that of the micro features.

3 CNN

3.1 Patch Size

The input of the CNN is a 3D array of size $[N_x \times N_y \times N_C]$ where: N_x and N_y are the size of the input image along the x and y direction respectively and N_C is the number of channels of every data point. Each data point has 4 channels namely σ_{xx} , σ_{yy} , τ_{xy} and *Geometry* corresponding to the xx , yy , xy component of the macro stress tensor and a binary image of the geometry respectively. We chose $R = 4$ so the input array is of size $[72 \times 72 \times 4]$. The output of the model is an $[N_x \times N_y]$ image corresponding to the micro Tresca stress, so here an image of size $[72 \times 72]$. Note that we are only interested in the ROI of the patch so all the statistics during training and inference are calculate in an $[32 \times 32]$ window in the middle of the patch as shown in [Fig 4]. Because we want to identify the effect of micro scale features on the macro scale stress we will scale the output with a number that reflects the intensity of the macro stress field. This number is the sum of the absolute principal stresses of the macro stress tensor $|\sigma_{\max}| + |\sigma_{\min}|$ from [Eq. 6]. The micro stress in areas away from micro scale features should be the same as the macro scale stress because these features only have a local effect. This suggests that the output should be constant away from the micro scale features and change rapidly very close to them. That is clearly visible in [Fig 6].

3.2 Scaling

Differences in the scales across input variables may increase the difficulty to model the problem, for example increased difficulty for the optimizer to converge to a local minimum or unstable behaviour of the network, thus a standard practice is to pre-process the input data usually with a simple linear rescaling [Bishop, 1995]. In our case we will scale the data not only to improve the model but also to restrict the space we have to explore. The space that we have to cover is infinite because the input can take any real value. Fortunately, Tresca stress scales linearly with the components of the stress tensor. From [Eq. 6] it is trivial to show that if we replace σ_{xx} , τ_{xy} , σ_{yy} to $k \cdot \sigma_{xx}$, $k \cdot \tau_{xy}$, $k \cdot \sigma_{yy}$ where k is some scaling factor, then $\sigma'_{\max} = k \cdot \sigma_{\max}$ and $\sigma'_{\min} = k \cdot \sigma_{\min}$ where σ'_{\max} and σ'_{\min} are the new principal stresses after scaling the input and thus $\text{Tresca}' = \frac{1}{2}(\sigma'_{\max} - \sigma'_{\min}) = \frac{1}{2}(k\sigma_{\max} - k\sigma_{\min}) =$

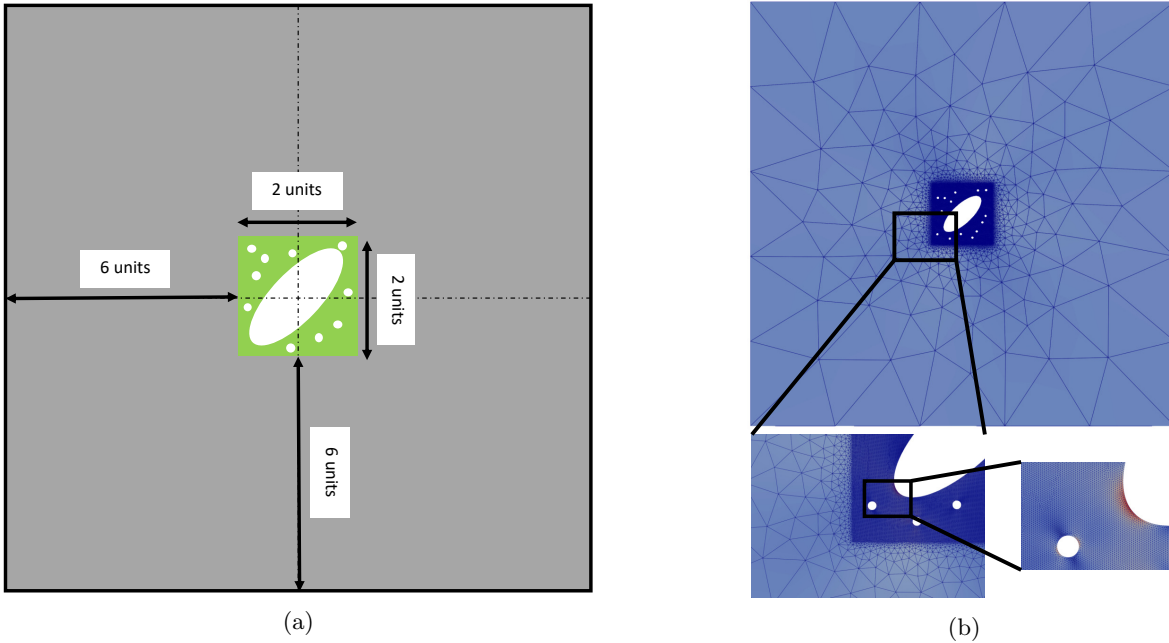


Figure 5: On the left (a), a sketch of buffer zone with grey and on the right (b) an example where the mesh and buffer area are visible.

$k \cdot \text{Tresca}'$ where Tresca' is the Tresca stress after scaling. Additionally, because we model linear elastic problems scaling the load terms with a scaling factor k will result in a local and global stress field multiplied by k as well. Here k^{-1} is the maximum stress value present in all the 3 stress components over the patch. This scaling of the input values to the range $[0, 1]$ allows us to make predictions on input data of any possible scale. We just have to calculate k , multiply the input by it to transfer it to the desired scale and then multiply the output with k^{-1} to get the true output.

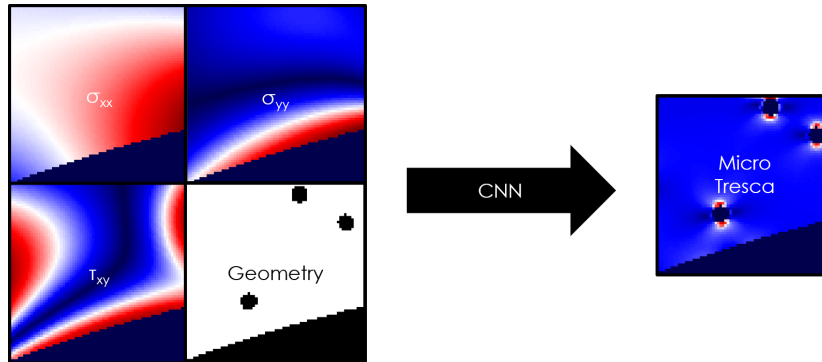


Figure 6: On the left the input of the CNN and on the right the output

3.3 Layers

Although Deep Neural Networks have been successfully used to model very complex tasks, their training is challenging for a number of reasons. In this work we will use two layers that will allow us to efficiently train our DNN namely Batch Normalization (BN) and Residual Blocks.

3.3.1 Batch Normalization

In DNNs the distribution of each layer’s inputs changes during training, as the parameters of the previous layers change, this phenomenon is known as internal covariate shift. This slows down the training by requiring lower learning rates and careful parameter initialization [Ioffe and Szegedy, 2015]. BN aims at reaching a stable distribution of activation values throughout training. To achieve that, BN normalizes the output of a previous activation layer by subtracting the batch mean and dividing by the batch standard deviation. After the normalization, BN tries to scale and shift the normalized output by adding two trainable parameters to each layer. [Ioffe and Szegedy, 2015; Santurkar et al., 2019]. Additionally, BN makes the optimization landscape significantly smoother. This smoothness induces a more predictive and stable behaviour of the gradients, allowing for faster training [Santurkar et al., 2019]. Lastly, there is a large consensus that the BN should be used before dropout and the activation function [Ioffe and Szegedy, 2015; Li et al., 2018a; Garbin et al., 2020]

3.3.2 Residual Blocks

Another problem with DNNs is the vanishing gradients causing the NN to not be able to learn simple functions like the identity function between input and output [Hochreiter et al., 2001; Sussillo and Abbott, 2015]. The current way to train DNNs is through residual blocks [He et al., 2015; Kim et al., 2016; Zagoruyko and Komodakis, 2017; Lim et al., 2017]. With residual blocks the NN itself can choose its depth by skipping the training of a few layers using skip connections. As we can see from [Fig 7] even if the NN chooses to ignore some layers ($F(X) = 0$) it will learn to map the input of the block to the output of the block. In this case the expression of the output would be simplified to: $F(X) + X = 0 + X = X$. This way we can use a large number of residual blocks and the network will simply ignore the ones it does not need. The name residual comes from the fact that the network tries to learn the residual, $F(X)$, or in other words the difference between the true output, $F(X) + X$, and the input, X .

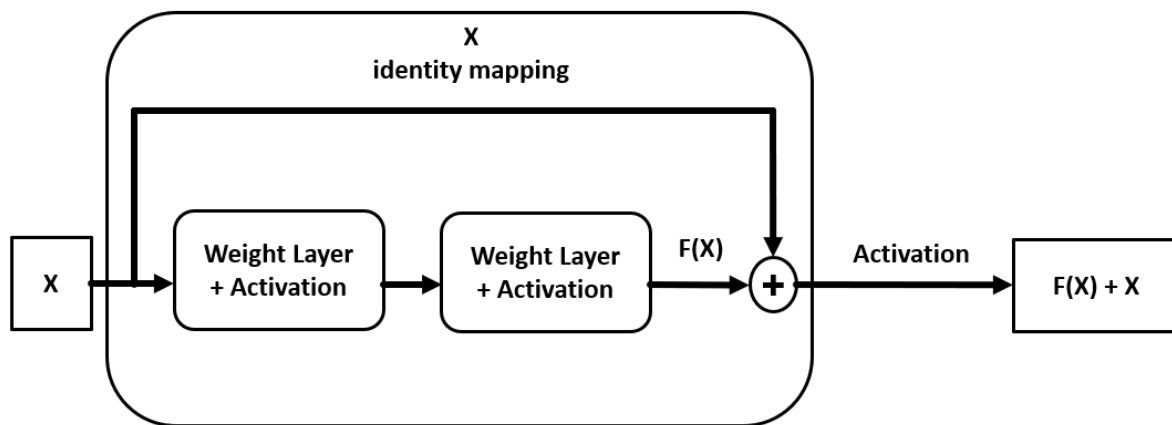


Figure 7: Structure of a generic residual block with input X and output $F(X) + X$.

3.3.3 Squeeze and Excitation block

In the residual blocks of our CNN we are using another kind of block: the Squeeze and Excitation block, SE. The SE can adaptively recalibrate channel-wise feature responses by explicitly modelling interdependencies between channels resulting in improved generalization across datasets and improvement in the performance [Cheng et al., 2018; Li et al., 2018b; Hu et al., 2019]. The input of the SE

has C channels, height H and width W , $[H \times W \times C]$. The input decreases in size using a global-averaging pooling layer resulting in a linear array of size $[1 \times C]$. After that, two fully connected layers downsample and then upsample the linear array. Firstly the linear array is downsampled by a factor of 16, $[1 \times C/16]$, as this is indicated to result in optimum performance [Hu et al., 2019], then a ReLU activation function is applied before upsampling again using a factor of 16 $[C/16 \cdot 16 = 1 \times C]$ and in the end a Sigmoid activation function is applied. Lastly, the linear array is reshaped to size $[1 \times 1 \times C]$ and multiplied with the input of the SE block [Fig 8].

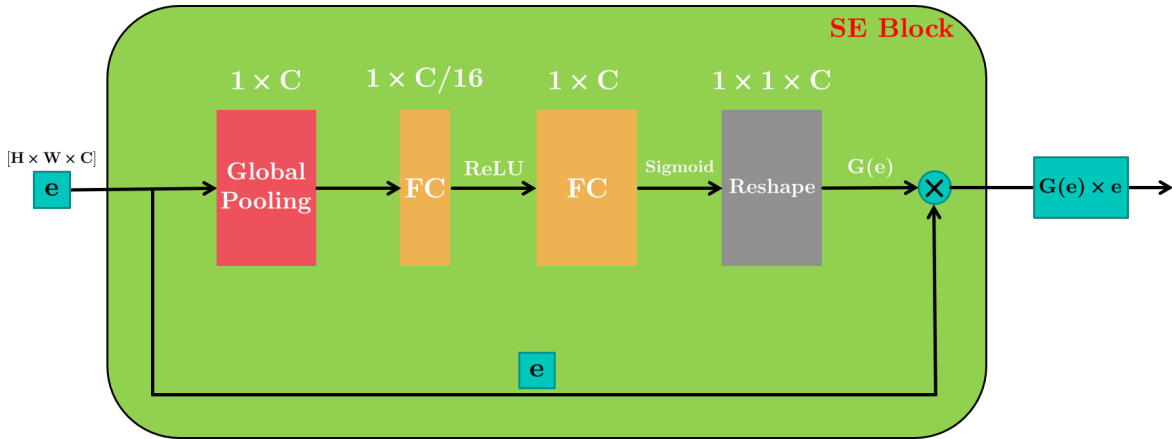


Figure 8: Structure of a generic SE block with input e and output $G(e) \times e$. FC stands for Fully Connected layer

3.4 Architecture

The residual blocks we will use in this work consist of two convolution layers, followed by a BN layer and a ReLU activation function each, and a SE block in the end [Fig 9]. The input and output of this block has exactly the same size as we choose the number of filters for the convolution layers to be the same as the number of filters at the input of the residual block.

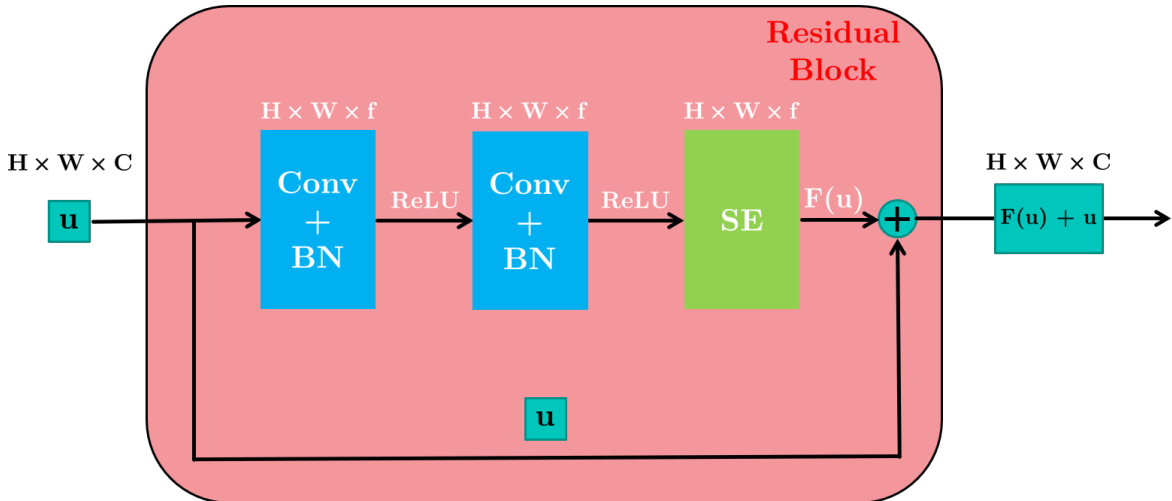


Figure 9: Structure of the residual block we are using with input u and output $F(u) + u$.

The architecture of the network is inspired by the “StressNet”, proposed by [Nie et al., 2019]. Three

convolution layers with increasing number of filters will downsample the input, after that five residual blocks are applied to the resulting array before using 3 deconvolution layers with a decreasing number of filters to upsample to the original dimension but with 1 channel instead of 4 [Fig 10].

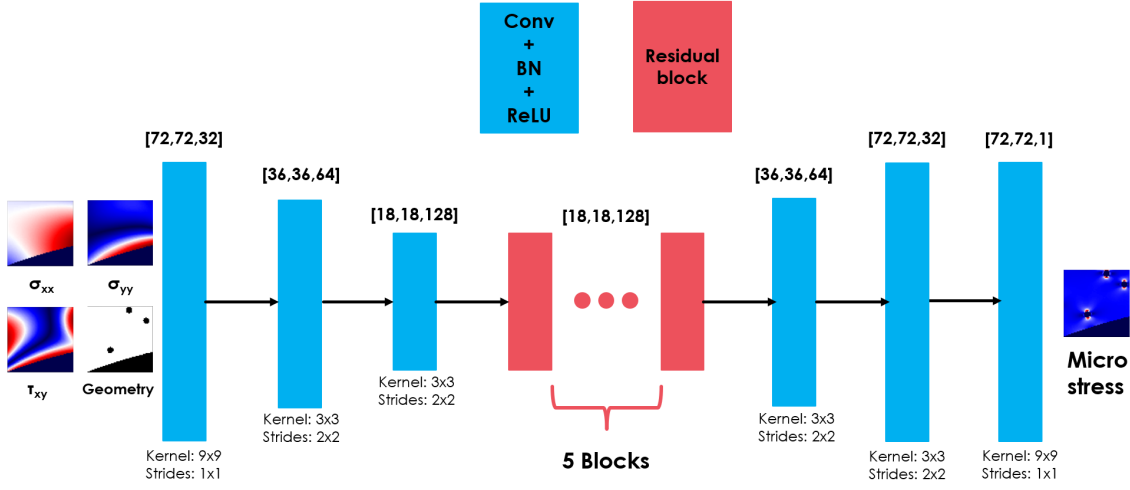


Figure 10: Structure of the CNN. σ_{xx} , σ_{yy} and τ_{xy} are the stress components on the x , y and xy direction respectively.

4 Bayesian Neural Network

4.1 Bayes By Backprop

In our effort to include uncertainty information into our prediction we will deploy a Bayesian framework, as described by [Blundell et al., 2015], to introduce uncertainty in the weights of the network. To achieve that we will replace the constant weights of a deterministic neural network with a distribution over each weight as seen in [Fig 11]. The output of this probabilistic model, for an input $x \in \mathbb{R}^n$ and a set of possible outputs $y \in \mathbb{R}$, will be a probability distribution over all possible outputs. The distribution of the weights before observing the data is called prior distribution, $P(w)$, and it incorporates our prior beliefs for the weights. The goal is to calculate the posterior, the distribution of weights after observing the data, because during training and of course inference the weights of the network are sampled from the posterior. The goal of Bayesian inference is to calculate the posterior distribution of the weights given the training data, $P(w|D)$. Unfortunately, the posterior is intractable for NNs but can be approximated by a variational distribution $q(w|\theta)$ [Hinton and van Camp, 1993; Graves, 2011], parameterised by θ . Variational learning finds the parameters θ^{opt} that minimise the Kullback-Leibler (KL) divergence between the approximate posterior and the true Bayesian posterior. This KL divergence between the approximate posterior and the true Bayesian posterior is the loss function and is defined as follows [Eq. 8]:

$$\begin{aligned}\theta^{opt} &= \arg \min_{\theta} \text{KL}[q(w|\theta)||P(w|D)] \\ &= \arg \min_{\theta} \int \log \frac{q(w|\theta)}{P(w)P(D|w)} dw \\ &= \arg \min_{\theta} [\text{KL}[q(w|\theta)||P(w)] - \mathbb{E}_{q(w|\theta)}[\log P(D|w)]]\end{aligned}\tag{8}$$

The first term of the loss is the KL divergence between the approximate posterior and the prior. It is obvious that the prior is introducing a regularization effect because the KL divergence penalizes complexity by forcing the approximate posterior to be close to the prior. The second part is the negative log likelihood. This is a data dependent term and it forces the network to fit the data.

Here we consider the approximate posterior to be a fully factorised Gaussian [Graves, 2011]. During one forward pass we sample the weights from the posterior but during back propagation we would have to define the gradient of the loss with respect to this sampling procedure, which is of course not possible. Instead we use the reparameterization trick [Kingma and Welling, 2014]. This procedure is well described in [Blundell et al., 2015]. Instead of having a parameter-free operation (sampling) we can obtain the weights of the posterior by sampling a unit Gaussian shifting it by a mean μ and scaling it by a standard deviation σ . This standard deviation is parameterised as $\sigma = \log(1 + \exp(\rho))$ and thus it is always positive. So the weights are sampled according to the following scheme: $w = \mu + \log(1 + \exp(\rho))$, and the variational parameters to be optimised are $\theta = (\mu, \rho)$.

4.2 Adapting the Bayes by Backprop method to our case

The architecture of the BNN remains the same as the deterministic case but we replace all the convolutional and dense layers with the respective Bayesian layers. We use a Gaussian as predictive distribution, $P(y|x, w)$, corresponding to a squared loss [Blundell et al., 2015]. We choose to have Gaussian distributions as priors which corresponds to L2 regularization [Blundell et al., 2015]. There is a single prior distribution for each layer, so all the weights in a layer share exactly the same μ and ρ . During backpropagation we optimise the prior by considering the gradients of loss not only with respect to the posterior but also the prior parameters. This allows us to change the prior hyperparameters of our model by using the available data, this process is known as empirical Bayes. In the results section we will demonstrate the advantages that empirical Bayes offers to our model. The mean prediction

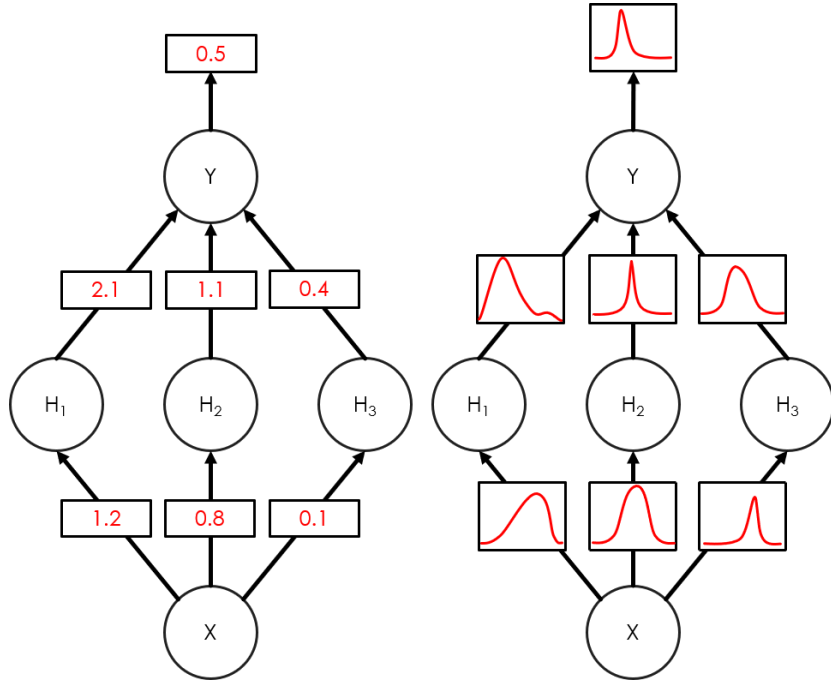


Figure 11: On the left we have a sketch of a plain Neural Network with constant weights and on the right a Bayesian Neural Network where the weights are replaced by distributions. In both sketches the biases have been omitted for simplicity.

and the variance for the Bayesian CNN are calculated by passing the same input through the network multiple times.

4.3 Selective Learning

A selective learning process, in a supervised learning framework, assumes that a large pool of unlabelled data is available while there is a very expensive function that labels this data. The aim of selective learning is to identify which of the unlabelled data contain useful information so that only these are labelled. To achieve that, an acquisition function needs to be formulated to identify the useful data. [Tsymbolov et al., 2018] suggest that the uncertainty extracted from a Bayesian Neural Network is a sensible acquisition function for this task. This is also intuitively a sensible conclusion because high uncertainty in the prediction of the network means that the input is far away from the training data distribution.

In our case the pool of unlabelled data is a large number of coarse scale FE simulations. The expensive function that labels these data is the fine scale FE simulations that take into account the micro features of the geometry. The aim of selective learning in our case is to identify the stress cases and/or microstructural patterns that are sufficiently different from the ones that are already in the labeled set and perform the fine scale FE simulations only to these cases. This is very important for our application because the cases that will be identified by the SL framework are exactly the cases that contain unknown interactions that our network would have predicted with a large error. For the acquisition function we need an uncertainty metric. Here we chose the max variance present in each prediction.

5 Results

5.1 Numerical Example with 1 Ellipse

Firstly we created an initial dataset with very simple examples [Fig 12]. A single ellipse in the middle playing the role of the macroscale feature, creating a diverse macroscopic stress field. Also, a few micro features are randomly positioned around the ellipse, accounting for the micro scale features that will affect the macro stress field. All the micro features have a circular shape and the same radius, $R = 4$ units. From 500 examples, generated in 43 hours, we extracted 33,000 patches, 5,000 of which were used as a validation set. No rotations were applied to this dataset as data augmentation technique. The patches were extracted such that the union of all the ROIs is equal to the entire domain Ω . Specifically, the ROI of the first patch is aligned with the top right corner of the domain and the rest of the patches are created using a sliding window and a stride equal to half the length of the ROI in each dimension. The patches that do not contain any micro or macro scale features are discarded.

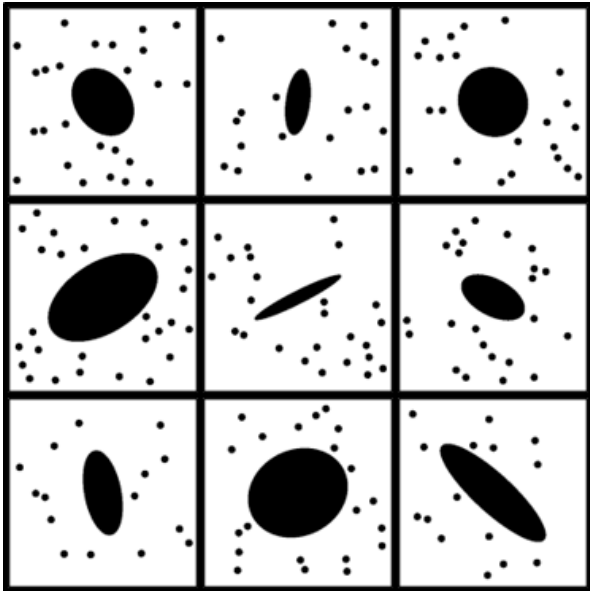


Figure 12: Nine examples from the initial dataset

Experiments on this dataset showed very positive results. Training with 28,000 data points and validating on 5,000 unseen data points resulted in a validation accuracy of 96% when training with the Adam optimizer for 600 epochs, which required about 6 hours on a NVIDIA T4 GPU. The loss function that we used is the mean squared error applied only in the ROI as already discussed. The concept of accuracy in a regression task with images needs to be discussed. The process followed to define accuracy is summarised in [Algorithm 1] and it is described with more detail as follows.

1. We take the max of each prediction in the ROI, this is because we are primarily interested in the max values as these values will indicate if the material will fail or not
2. We define an error metric between the real max value, y_{FE} , and the max value in our prediction, y_{NN} . Here we use the relative error defined as: $relative_error = |y_{NN} - y_{FE}|/y_{FE}$
3. We set a threshold for the acceptable error. In this case we will use 10%. To sum up, 96% validation accuracy means that in the validation set 96% of the max values in the ROI were predicted with a relative error less than 10%

Algorithm 1 Calculate accuracy

```
1:  $N = \text{length}(\text{datapoints})$ 
2:  $\text{accepted} = \text{zeros}(N)$ 
3: for  $\text{point}$  in  $\text{datapoints}$  do
4:    $y_{NN} = \text{max}(\text{prediction}[\text{point}])$ 
5:    $y_{FE} = \text{max}(\text{ground\_truth}[\text{point}])$ 
6:    $\text{error} = |y_{NN} - y_{FE}|/y_{FE}$ 
7:   if  $\text{error} \leq \text{threshold}$  then
8:      $\text{accepted}[\text{point}] = 1$ 
9:  $\text{accuracy} = \text{sum}(\text{accepted})/N$ 
10: return  $\text{accuracy}$ 
```

This 10% threshold is arbitrarily chosen and it should be more application specific because different applications have different error requirements. We have constructed a diagram that shows the accuracy as a function of the threshold [Fig 13].

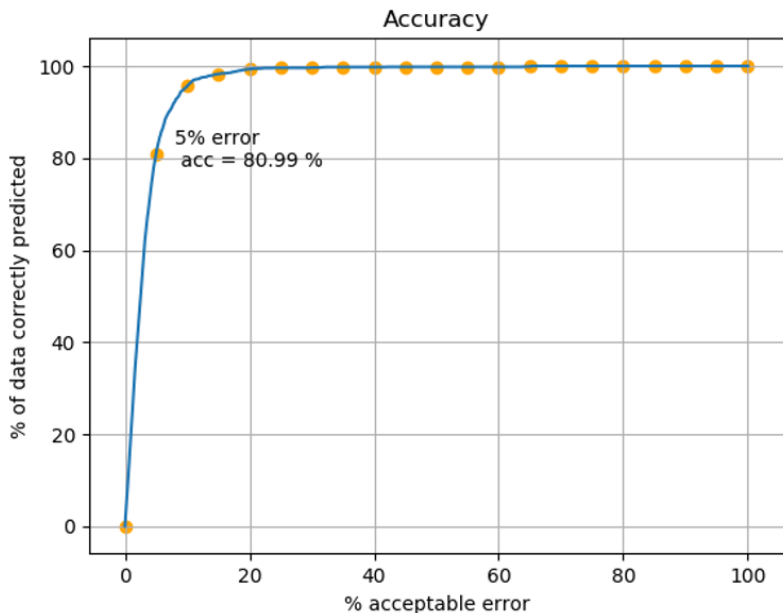


Figure 13: Accuracy as function of the threshold

We present results from 2 random patches [Fig 14] and then a result on the whole structure [Fig 15]. For the whole image the true Tresca is displayed and not the scaled version of it. The prediction is made again on the patch level but then the original image is reconstructed. This is possible if we align one corner of the ROI with a corner of the image and use a sliding window equal to the size of the ROI as can be seen in [Fig 16]. We can see that in all cases the CNN was able to accurately reconstruct the full micro stress field but it was also able to predict the max values with a very small error. More specifically it is clear that away from the micro scale features the micro scale field is constant. We can also see that very close to the micro scale features we have a very steep rise of the micro Tresca stress. The micro stress field is accurately predicted even in complicated cases where more than one micro features are interacting or micro features and macro scale features are interacting.

Lastly, we will investigate the effect of training with less data on the CNN accuracy. We randomly

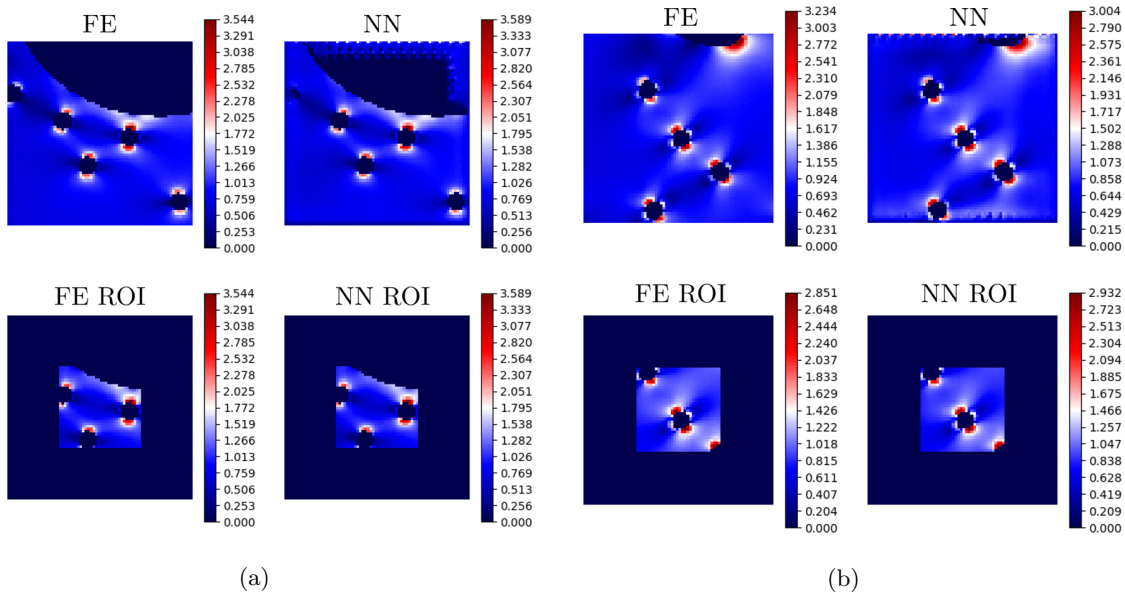


Figure 14: Prediction of the Network on 2 patches. On the top left of each example we see the FE result for the whole patch and on the top right the NN prediction for the whole patch. On the second row we see the same but for the ROI.

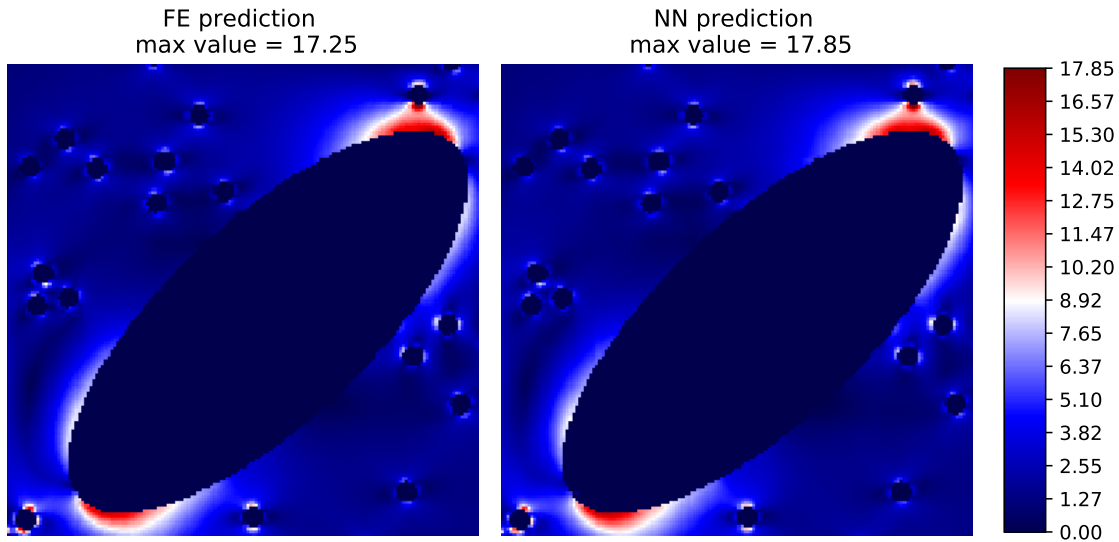


Figure 15: Comparison between the FE solution, on the left, and an image reconstructed using the NN predictions, on the right.

chose 10,000 data points, almost 30% of the available data, and train the NN with exactly the same settings, an example can be found in [Fig 17]. We noticed that for the 10% threshold the accuracy is 6% higher for the large dataset even though we used almost 3 times as much data. This may look like a small increase but it means that the mispredicted cases climbed from 4% to 10%. In reality most of the data that we rejected when we created the smaller training dataset (10,000 datapoints)

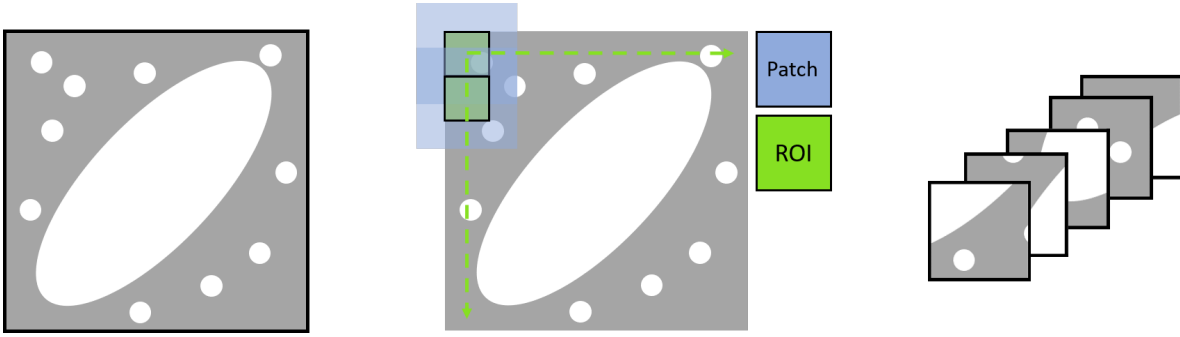


Figure 16: Patch generation for full image prediction. The corner of the ROI is aligned to the corner of the image and then a sliding window of size equal to the size of the ROI is used.

were very similar to the ones accepted in the smaller dataset. A small portion of them contained new interactions that our network would have learned from. These cases are exactly the cases we are interested in because they contain complex examples that create strong interactions and sharp increase in the micro stress field. In section [5.4] we will demonstrate a Selective Learning framework that will allow us to identify these cases and train our network only on them. This way we keep the computational cost to the minimum while preserving the same level of accuracy.

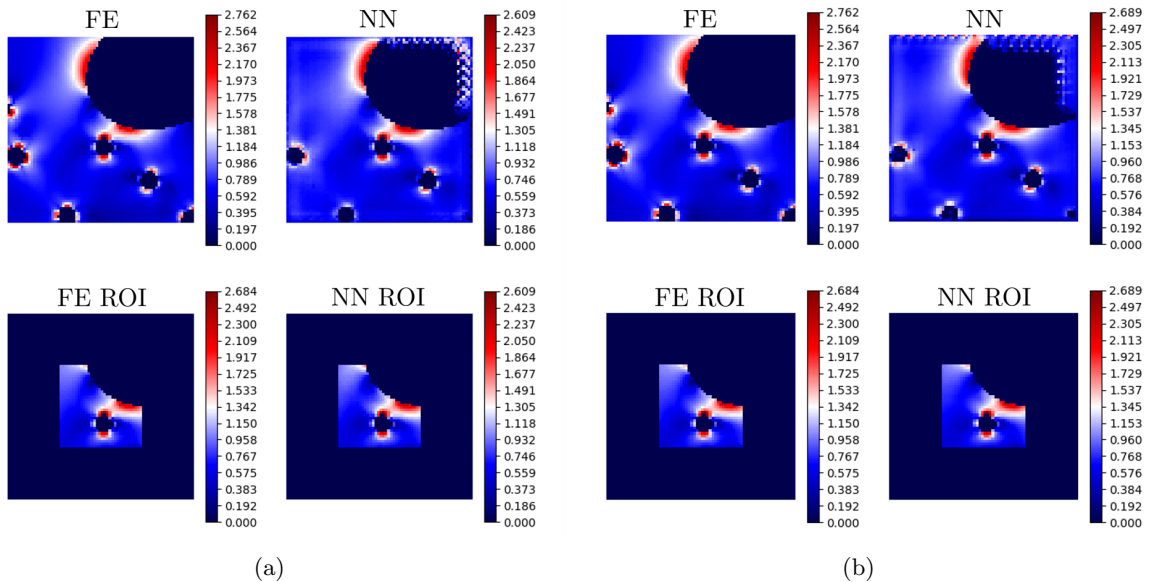


Figure 17: A prediction for the same input for 2 identical NNs trained with 10,000 data points (a) and 28,000 (b). The two ROI predictions look very similar but we can observe that the maximum predicted value from the NN that was trained with the larger dataset is closer to the real value compared to the maximum predicted value from the NN that was trained with the smaller dataset.

5.2 Numerical Example with 3 Ellipses

Even though the CNN we trained seems to work well for the data it was trained on we do not expect the same level of accuracy as we depart from this dataset, although the method is fully non-parametric

and the trained NN can make prediction for any unseen micro and macro geometries. Specifically, we would expect a decrease in accuracy in the following cases.

1. Spatially fast varying macro stress field, generated by macroscale features not present in the training dataset
2. Microscale features not present in the training dataset, for instance non circular holes
3. Patterns of microscale features not present in the training dataset, for instance different distribution of circular holes

To tackle this problem we created a new, more interesting, family of data with the expectation that this would add more complexity [Fig 18]. At first, we used the old CNN to make predictions on the new dataset. We observed that the accuracy dropped from 96% to 72%. This implies two things. Firstly, the drop in accuracy means that the new dataset contains information that the network had never seen before or was unable to learn from (due to the sparsity of the examples), thus training in this dataset will help the CNN to generalize better. Lastly, the concept of making the knowledge transferable seems to be working as we were able to make reasonable, but not perfect, predictions on a new family of data. This suggests that we managed to learn interactions between micro scale features and the macro stress field and not just the structures themselves.

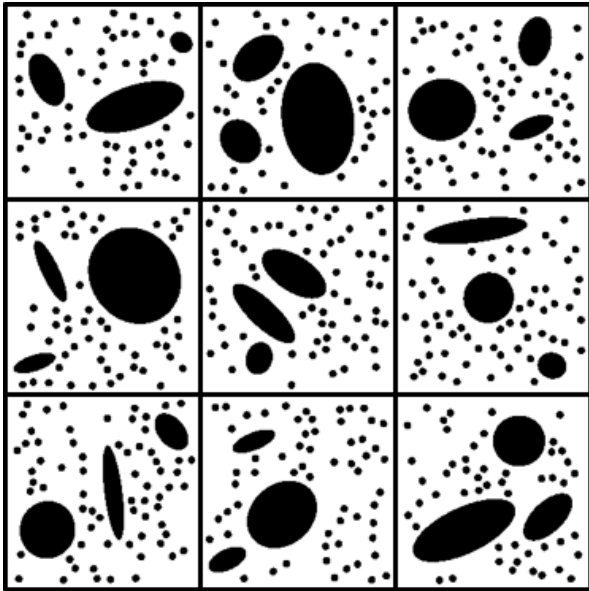


Figure 18: Nine random examples from the advanced dataset

Training a CNN with the new dataset proved to be more challenging. By using 23,000 training data points (almost as many as with the original case) and 5,000 validation data points we obtained, with the same settings, a validation accuracy of 74% in contrast to the 96% in the first case. We believe that this happens not only because more micro scale features are present in each case but also because the 3 ellipses are creating a much more complicated macro stress field. From experiments we found out that, as more and more new data points are added, the accuracy tends to increase slower and slower. This happens because the new data points added tend to contain less and less new information. We can use rotation as data augmentation technique, by rotating mechanically the stress [Eq. 2] and “physically” the images. We started from an initial training set of 5,000 data points ($\approx 1/4$ of the full set) and we rotated the dataset 6 and 12 times. After training with the same settings for all the cases, a validation

accuracy of 62%, 80% and 82% was achieved for the 0, 6, 12 rotations dataset respectively for the 10% threshold [Fig 19]. Firstly, this means that we managed to outperform by 8% the full dataset and secondly, we realized that rotating from 6 to 12 times didn't add a significant amount of new information even though the data are doubled. Once more, that was the motivation to start working with Selective Learning. We can see an example of a prediction with all 3 CNNs on the same input [Fig 20], where the prediction improves with the number of rotations. We can also see a prediction of the CNN trained with 6 rotations on 4 random patches [Fig 21].

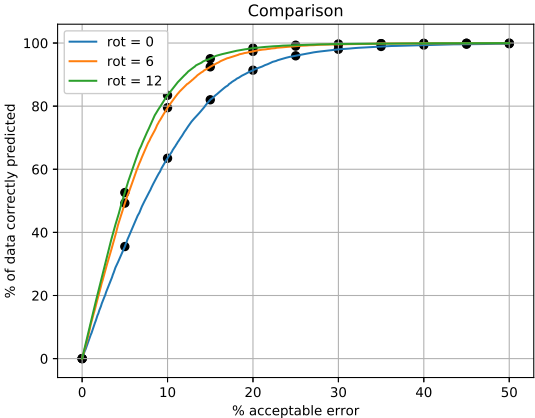


Figure 19: Comparison between 3 CNNs trained with the same settings but different datasets. Blue line corresponds to the original dataset with no rotation, orange line to a dataset with 6 rotations and finally the green line to a dataset with 12 rotations. We can observe that the accuracy increases as the number of rotations increases.

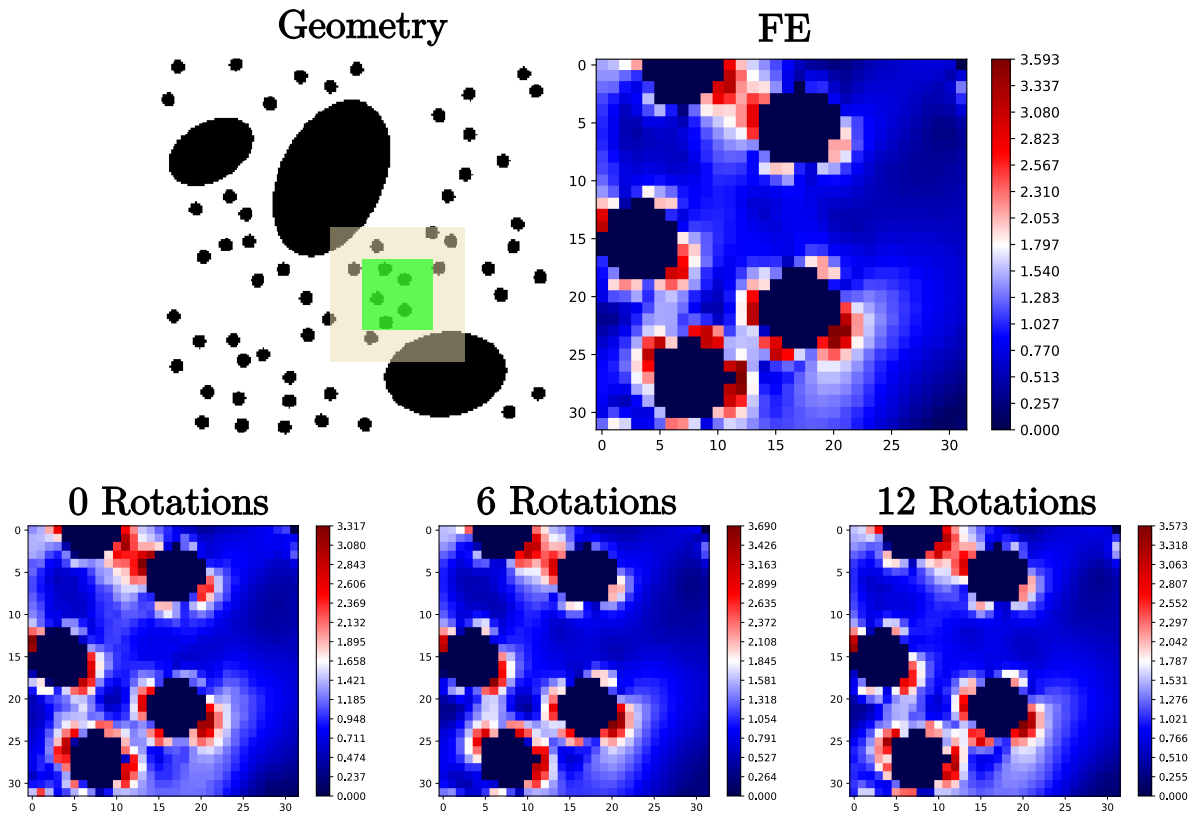


Figure 20: Top left corner the structure, the patch (with light brown) and the ROI (with green) for the prediction. Top right corner the FE solution in the ROI. Bottom from left to right, prediction in the ROI from a NN trained with a dataset with 0, 6 and 12 rotations respectively. We observe that even though those 3 images look quantitatively very similar the predicted maximum value approaches the one calculated by the FE simulation as the number of rotations increases.

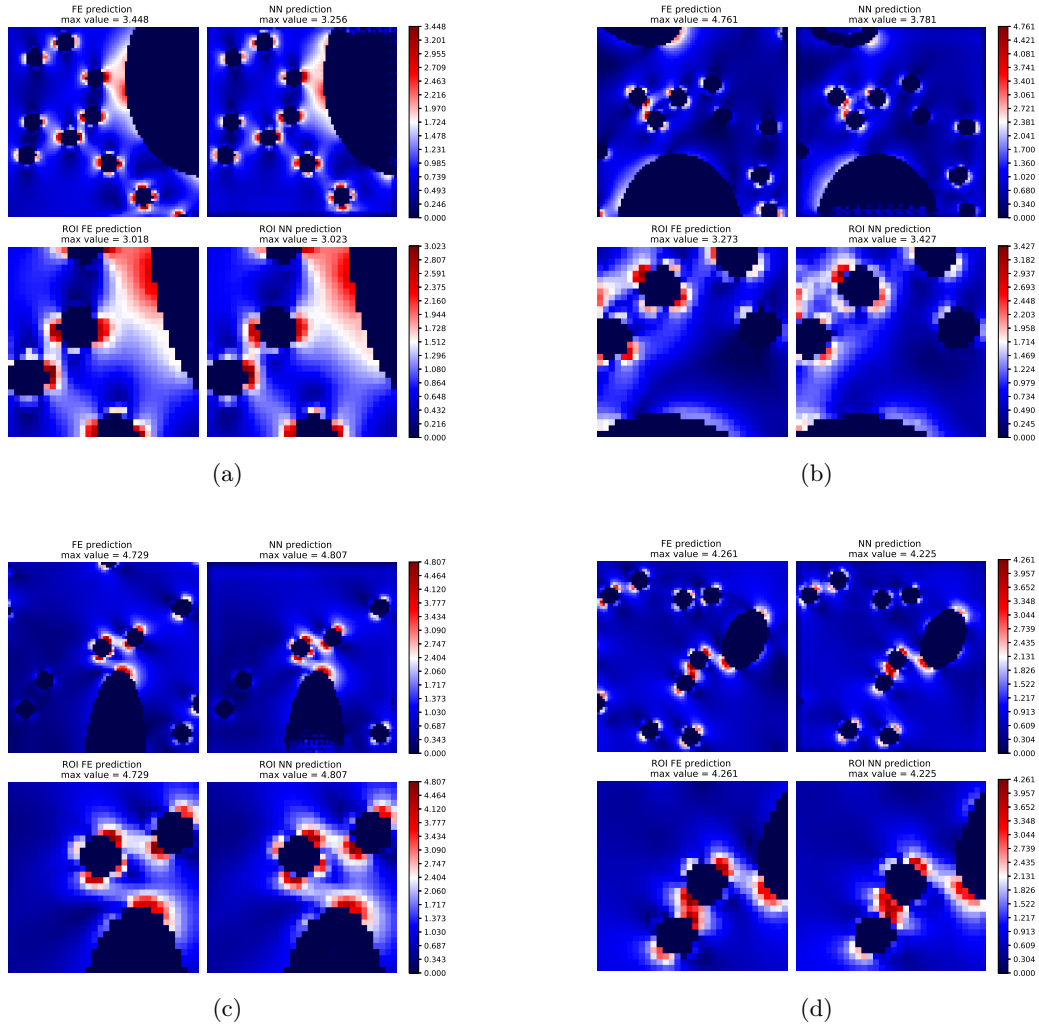


Figure 21: Prediction of the CNN trained on the 6 rotation dataset on 4 patches. In each of the 4 images, on the first row we can see the FE solution for the entire patch on the left and the NN prediction for the entire patch on the right. On the second row we can see the FE solution for the ROI on the left and the NN prediction for the ROI on the right. In all four cases we have strong interactions between micro scale features and in images (a), (c) and (d) we have strong interactions between micro and macro scale features. We can see that in all the cases the prediction in the ROI is qualitatively very similar to the FE simulation but also that the prediction for the maximum value in the ROI is very close to maximum value in the ROI calculated by FE simulations.

5.3 Numerical Example using a Bayesian Neural Network

Until now we have used a deterministic neural network for the predictions. In this section we will present results corresponding to the use of the Bayesian NN. We trained the BNN with the same 5,000 data points as in section [5.2] for 600 epochs and validated on 10,000 data points. That requires 2.1 times more computational time compared to the deterministic case. The accuracy of the prediction is 72% for the 10% threshold compared to 62% for the deterministic case. In the Bayesian CNN case the accuracy is calculated using the MAP solution.

The mean and the variance of the BNN prediction are calculated by drawing the weights of the network from the posterior distribution 100 times and performing inference for every input. The results for a BNN where the prior was optimised during training can be found in [Fig 22]. We can see from the first image, [Fig 22a], that the mean prediction is very close to the real value. We can also observe that for higher values we get higher absolute error. This is expected because those cases are represented to a lesser extent in the dataset. In the second image, [Fig 22b], we can observe that the diagonal is almost always, and specifically for 92% of the data points, between the upper and lower 95% Credible Intervals (CIs) implying that the true solution is bounded by the 95% CIs for 92% of the data points. Lastly, we can observe a BNN where the prior parameters were not optimised during training. From [Fig 23a] we can see that the mean prediction is very good, a slight decrease of 2% is observed in the accuracy compared to the optimised prior BNN. Nevertheless, from [Fig 23b] and [Fig 23c] we can see that the uncertainty fails to explain the error as there are many cases where the diagonal is either above the upper 95% CI or below the lower 95% CI. Specifically, the true value is bounded by the 95% CIs in 82% of the cases, a decrease of 10% compared to the optimised prior BNN.

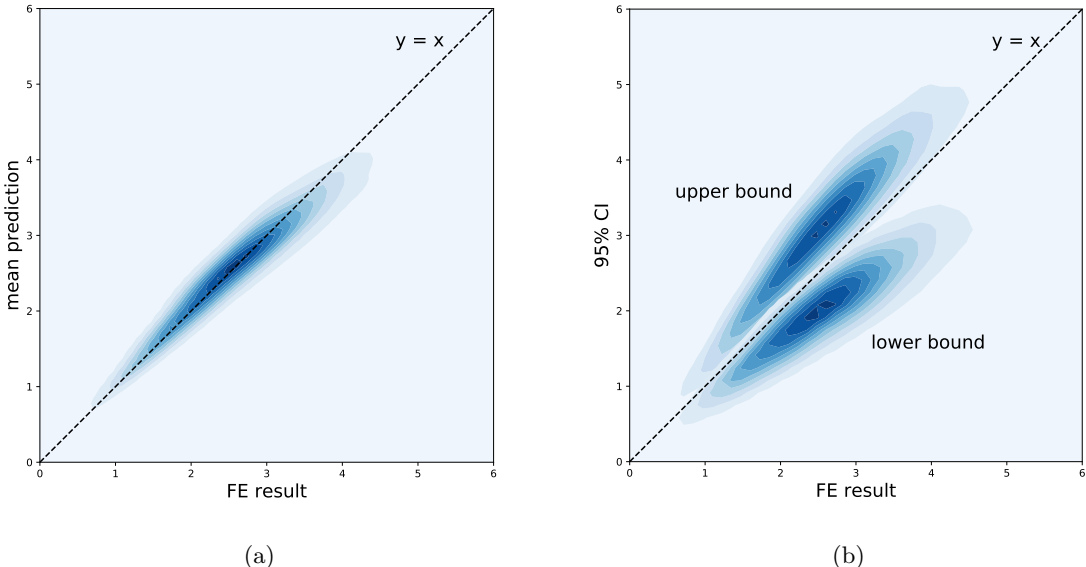


Figure 22: In these 2 figures we see point densities where darker colors correspond to higher point density. On the left (a), a diagram showing the relationship between BNNs’ mean prediction and FE results for the maximum value in the ROI. We can clearly see that most of the points are on the diagonal. On the right (b), a diagram showing the upper and lower 95% CIs for the prediction. We can observe that for most of the points the diagonal is between the upper and lower 95% CIs.

Results from the uncertainty estimation on image level can be found in [Fig 24]. On the top 2 cases [Fig 24a, 24b] we can see some examples of good mean predictions where there are clear interactions between multiple micro scale features. The middle images [Fig 24c, 24d] are examples of good mean

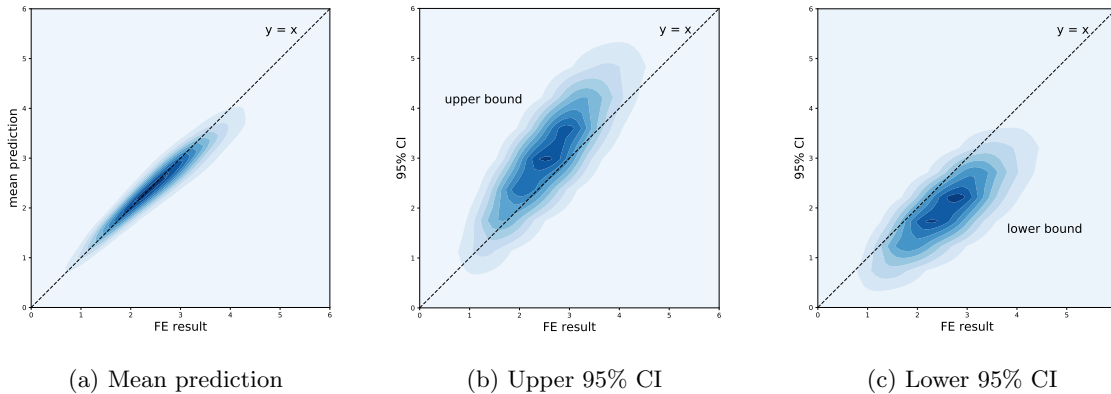


Figure 23: Three diagrams, depicting point densities where darker colors correspond to higher point density, corresponding to a BNN where the prior was not optimised during training. The prior distributions are Gaussian initialised as: $N(0, 1)$. First diagram (a) is the BNNs’ mean prediction against the FE results for the maximum value in the ROI. Most of the points are on the diagonal so the NN was able to provide good mean estimations. The next two diagrams correspond to the upper 95% CI (b) and the lower 95% CI (c). Ideally the point densities shouldn’t intersect with the diagonal. The high percentage of points below the diagonal for (b) and above the diagonal for (c) indicates that the network wasn’t able to successfully quantify the uncertainty.

predictions where interactions between multiple microscale features and a macro scale feature can be seen. We can observe that the uncertainty, expressed as $1.96 \times$ standard deviation, is higher in the vicinity of the higher error pixels indicating that the BNN has successfully identified the unseen interactions (interactions that were not in the training dataset or were underrepresented). [Fig 24e] is an example of a case where the maximum value is miss-predicted with a large error of about 1 unit. Fortunately, we can observe that the uncertainty is also very large, specifically $1.96 \times$ standard deviation has a value of about 1.5 unit meaning that the true maximum value is between the mean prediction and the 95% CI. Image [Fig 24f] is an example of a case with low uncertainty and low error. This means that the CIs are very tight and the BNN is very confident about the prediction. That was an expectable result in the sense that this is a very simple case, 2 circular micro scale features are weakly interacting, and we would expect from the BNN to handle it without a problem because the training dataset contains a huge number of these examples.

5.4 Selective Learning

In this section we investigate the idea of Selective Learning to reduce the labelled data requirements for training the BNN. We need an initial dataset with labeled data so we can initially train the BNN, a bigger dataset with only unlabeled data and finally a validation set with labelled data. The principles of this framework are described below.

1. We use an acquisition function to select small batches from the unlabeled dataset
2. We label the selected data points and “move” them to the training set
3. We train the BNN with the new training dataset
4. We measure the accuracy of the BNN using the validation set
5. We repeat the same process until the accuracy converges or we label the entire unlabeled set.

We designed a small experiment to validate our approach, inspired by [Gal et al., 2017]. Here we make a comparison between a network trained using the max uncertainty acquisition function, choosing first the points with higher uncertainty, and a second one trained using the random acquisition function, that chooses data points randomly. For the random selection approach we repeated the experiments 5 times and presented the mean and the 95% confidence interval. We used the following setup: 2,500 data points for the initial set, 2,500 data points as the unlabeled set and 11,000 data points as validation set. We trained each network for 50 epochs, we performed 50 forward passes for the uncertainty estimation and we added 500 data points in the labeled set at each iteration, query rate = 500. The accuracy is calculated from the mean prediction of the network. The results can be found in [Fig 25]. We observe that the results produced by the max uncertainty acquisition function consistently present higher accuracy. More specifically, with this unlabeled data set we can reach an accuracy of about 75%. This can be achieved using 1,500 points with the max uncertainty acquisition function but requires all the 2,500 if we choose points randomly. This means that we reduced the labeled data requirement by 40%.

Now we will use a larger unlabelled dataset consisting of 10,000 data points. We compare again the max uncertainty acquisition function and a random acquisition function. The initial training set has 5,000 data points. We train for 150 epochs every network. We perform 100 forward passes for the uncertainty quantification and we label 2,000 unlabeled data points at each iteration, query rate = 2,000. The results can be found in [Fig 26]. The accuracy increases faster for the max uncertainty acquisition function and also the loss function is decreasing faster until it reaches 6,000 new data points. At this point the accuracy practically stops increasing and the loss gradually approaches the same value as with the random acquisition function. Using the max uncertainty acquisition function we can reach the max accuracy using 6,000 data points while we need all the 10,000 data points when randomly choosing new data. Again we have a decrease of 40% in the labelled data requirement.

This time we want to perform a similar experiment but we are interested in examining the effect of query rate on the results. Specifically, we will use an initial set of 5,000 data points and we will perform Selective Learning on an unlabeled dataset of 4,000 data points. We will repeat the experiment 3 times, with query rates 500, 1,000 and 2,000. A similar experiment was conducted by [Islam, 2016], where he concluded that using very small query rates results in sub-optimal performance, higher simulation times and noisy behaviour. There are two reasons why the results are worse in this case. Firstly, adding only a few data compared to the size of the initial dataset might result in overfitting and secondly, these data points might get smoothed out in the loss function. The simulation time increases because the network needs to be retrained a considerable number of times. On the other hand using too large query rates also results in worse results because the weights of the network are not updated frequently enough so new information is rarely incorporated in the network and we end up again labeling and training on data points that do not contain new information. The results of our experiment can be found at [Fig 27]. We have reached the same conclusions. When query rate is 1,000 we have the optimal behaviour, when we double it we observe slower convergence and when we use a small query rate we observe noisy sub-optimal behaviour.

After validating the Selective Learning framework we will now use it without the random acquisition function as baseline. We will use all the 30,000 available data to train the network. As initial set we will use again 5,000 data points. We will query 5,000 unlabeled data points at each iteration chosen by the max uncertainty acquisition function. We will train for 300 epochs and perform 100 forward passes for the uncertainty quantification. The results can be found in [Fig 28]. It is clear that the accuracy is not improving after the third iteration, 15,000 data points, but we continued labelling points only for demonstration reasons. The mean squared error decreases for the first 3 iterations and then stops decreasing as well. In this example we could reach the maximum accuracy using 15,000 out of the 30,000 data points, so we managed to reduce the labelled data requirements by 50%.

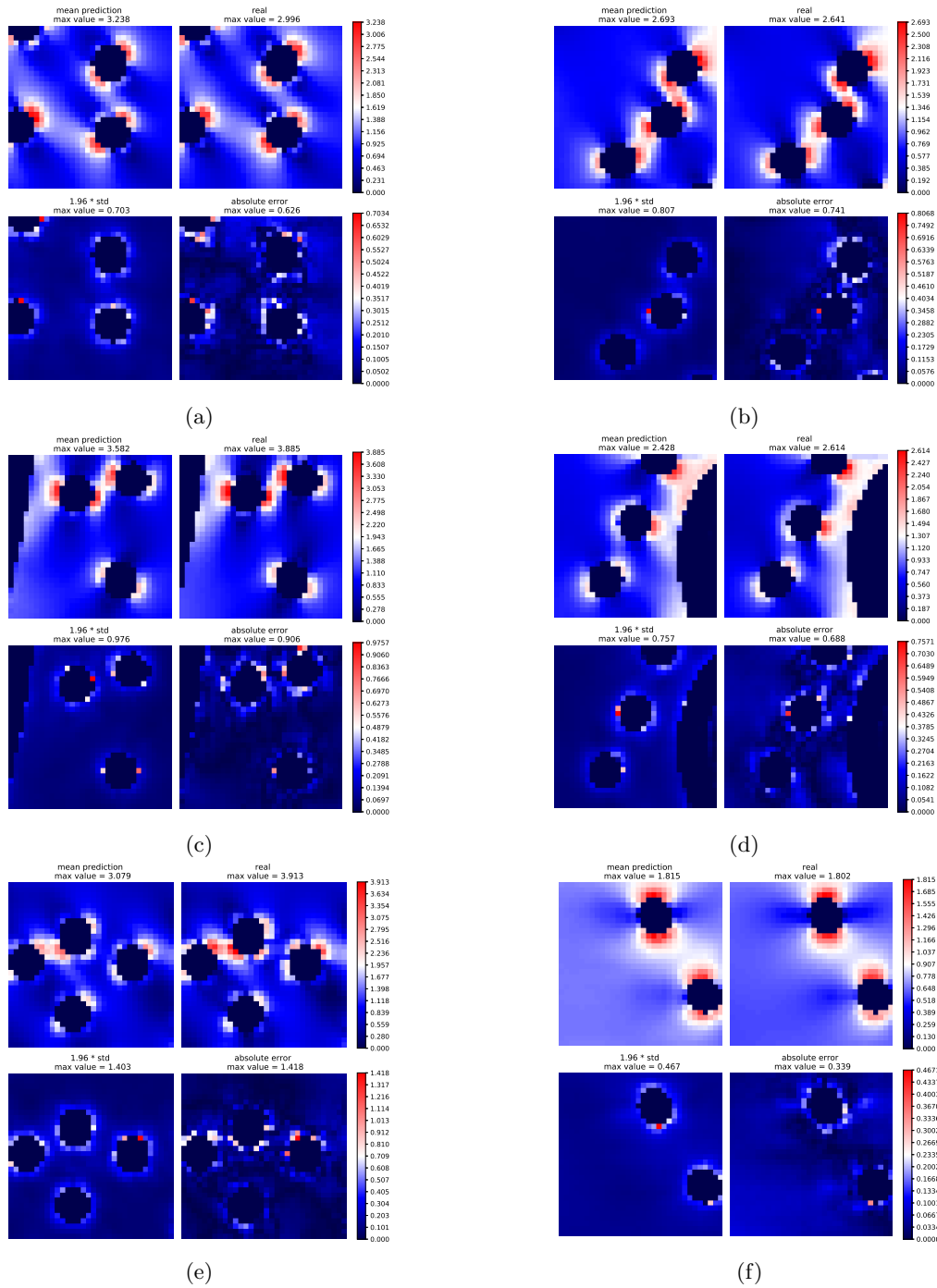


Figure 24: Examples of BNN predictions. All images correspond to the ROI of the patches. For each of the 6 images the first row corresponds to the NN mean prediction on the left and to the FE result on the right. The second row corresponds to the NN uncertainty, expressed as $1.96 \times$ standard deviation, on the left and to the absolute error between the NN mean prediction and the FE results on the right. In images (a) and (b), we can see strong interactions between micro scale features and in images (c) and (d) we can see strong interactions between macro and micro scale features. In all these cases we can observe that the uncertainty is higher in areas where the error is higher. In image (e) we observe that the error is very high but the NN was able to identify it and provided high uncertainty for the prediction. Lastly, in image (f) we observe an image with low error and low uncertainty.

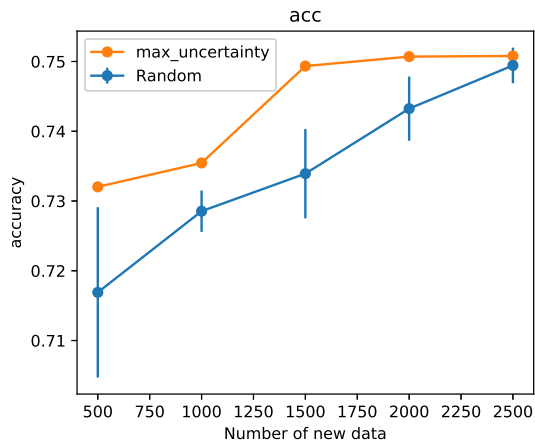


Figure 25: Results of Selective Learning for an initial set of 2,500 datapoints. 50 epochs per training, 50 forward passes for the uncertainty quantification and 500 added data in each iteration. The orange line corresponds to the max uncertainty acquisition function and the blue to the random acquisition function. For the random acquisition function we repeated the experiment five times and reported the mean values and the 95% confidence interval. We can observe that the orange curve is consistently above the blue one. This means that with the maximum uncertainty acquisition function we can achieve high accuracy with less data. Specifically in this case by using only 1,500 labelled data we achieve accuracy of about 75% with the maximum uncertainty acquisition function while we need to use all the 2,500 datapoints to achieve the same accuracy with the random acquisition function.

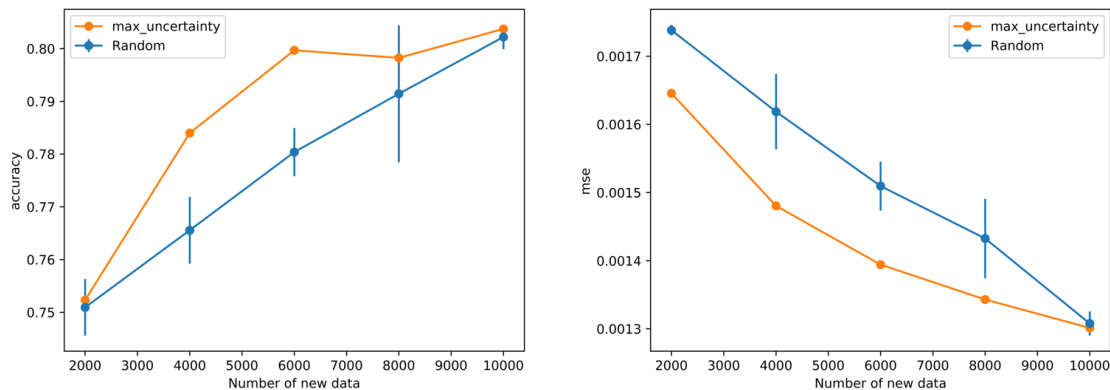


Figure 26: Demonstration of the selective learning framework for an unlabelled set of size 10,000 datapoints. On the left a diagram depicting the accuracy and on the right a diagram depicting the loss. The orange line corresponds to the max uncertainty acquisition function and the blue to the random acquisition function. For the random acquisition function we repeated the experiment five times and reported the mean values and the 95% confidence interval. For the accuracy we can see that the orange line is consistently above the blue line. Specifically, we can see that we can achieve a decrease of 40% in the labelled data requirement because the orange line reaches 80% accuracy with only 6,000 datapoints while the blue one with 10,000. For the loss we can see similar results where the loss for the maximum uncertainty case is consistently below the loss for the random case.

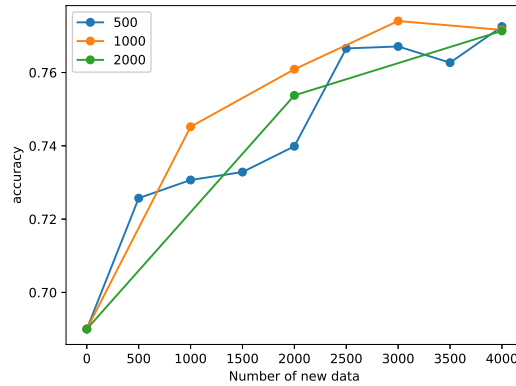


Figure 27: Selective learning with query rates of different sizes. The green line corresponds to a large query rate (of size 2,000 data points), the orange line to a medium query rate (of size 1,000 data points) and the blue line to a small query rate (of size 500 data points). The small and larger query rates result in sub-optimal behaviour and specifically small query rates result in noisy results.

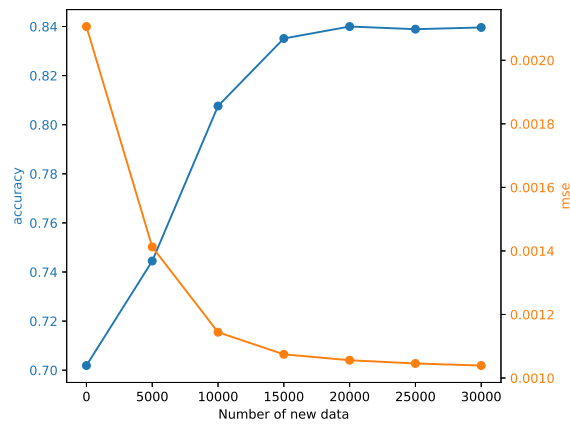


Figure 28: Accuracy and mean squared error plots with respect to train data chosen by a maximum uncertainty acquisition function. The blue line corresponds to the accuracy and the orange one to the mse. The accuracy initially sharply increases until reaching 15,000 labelled data points and after that no further increase is observed. The same can be seen for the loss that sharply decreases until reaching 15,000 labelled data points and then no further decrease is observed. In this case we can reduce the labelled data requirements by 50% if we only choose the first 15,000 data points indicated by the maximum uncertainty acquisition function and not the entire dataset of size 30,000 data points.

5.5 Out of distribution study

Lastly, we want to test the BNN in data outside of the training set. One way to realise this study is to keep the same micro scale features and create new micro distributions. That could be done using the “1 Ellipse Dataset” from section [5.1] and drawing data points from the “3 Ellipses Dataset” from section [5.2], to obtain out-of-distribution samples. Instead, we choose to completely change the micro scale features as we believe that this will be more challenging for the network to predict.

In this study we will use ellipses as micro features to get out of distribution samples. Neural Networks extrapolate when they make predictions outside of the data set and they are notoriously bad at extrapolating. What we are hoping for is that the BNN will understand that the ellipses are not in the dataset and will assign high variance to most of the patches.

We created 500 patches and made a prediction with the previous BNN. The results can be found in [Fig 29]. From the first plot [Fig 29a] we can see that the mean prediction from the BNN for the max values in the patch is not close to the real max value for a big percentage of the data, accuracy $\approx 50\%$, but is not unreasonable. Nevertheless, in a lot of cases the network successfully identified the interactions produced by the ellipses even if it was never trained on these. On the other hand, the second plot [Fig 29b] shows that in most cases, $\approx 80\%$, the true max value is indeed inside the 95% CI. Even more encouraging is the fact that higher uncertainty corresponds to higher error as can be seen from [Fig 30]. This also implies that selective learning is very promising in this case.

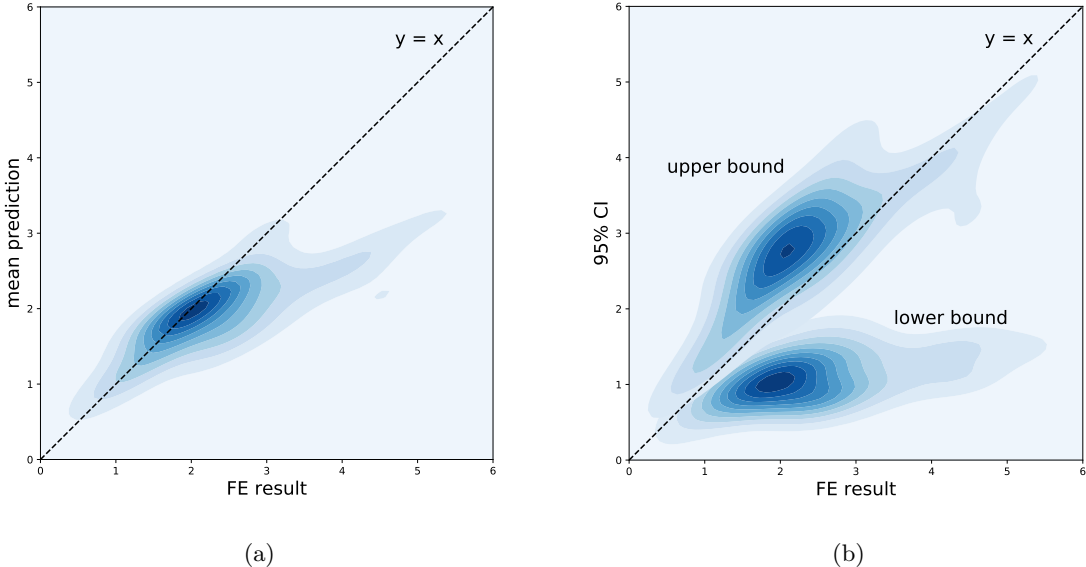


Figure 29: In these 2 figures we see point densities where darker colors correspond to higher point density. On the left a diagram (a) showing the relationship between NNs’ mean prediction and FE results for the maximum value in the ROI. We can observe that the maximum value is underestimated in a lot of data points from the BNN. On the right (b) a diagram showing the upper and lower 95% CIs. We can observe that in most cases the real maximum value is inside the 95% CIs of the prediction.

We can also see examples of predictions in 6 patches of this new dataset. In [Fig 31a, 31b] we can see 2 examples of cases where the error in max values is relatively high and even though the 95% CIs are very broad they fail to contain the real value. In [Fig 31c, 31d] we can see 2 examples of cases where the error is high but inside the 95% CI. Lastly in [Fig 31e, 31f] we can see 2 examples where the mean prediction of the BNN is very close to the real value. Some error is present in other areas of the patch but this error is captured by the uncertainty of the BNN.

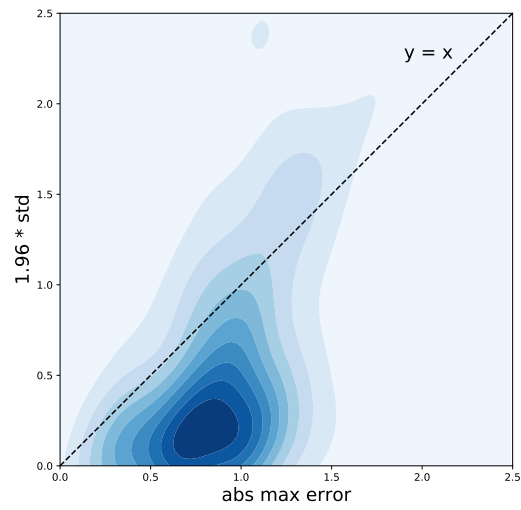


Figure 30: A diagram where the x axis is the absolute error between the real maximum value in the ROI and the predicted one and the y axis is $1.96 \times$ the standard deviation. We can observe a correlation between high uncertainty and high error.

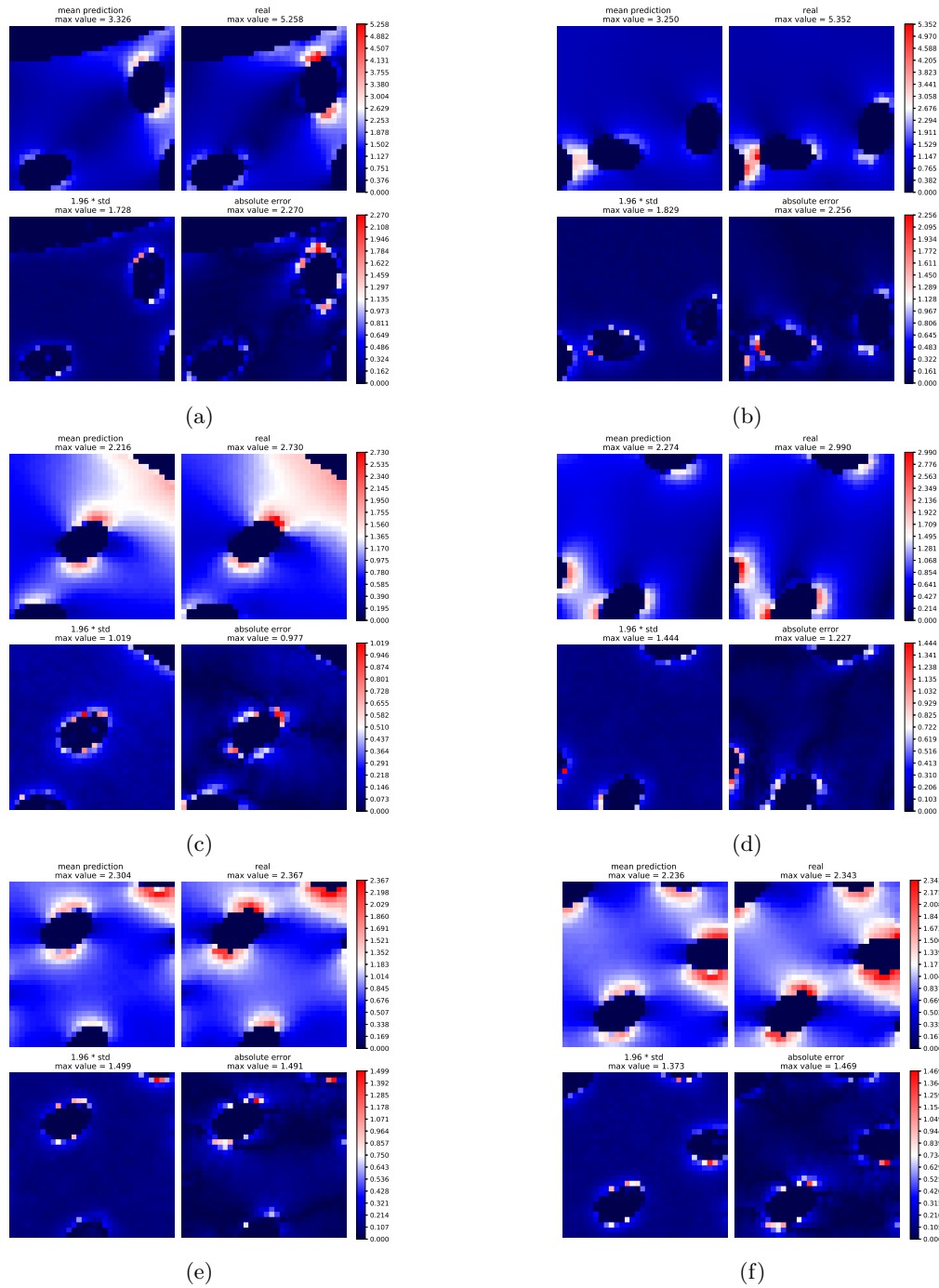


Figure 31: BNN predictions on out of distribution examples. All images correspond to the ROI of the patches. For each of the 6 images the first row corresponds to the NN mean prediction on the left and to the FE result on the right. The second row corresponds to the NN uncertainty, expressed as $1.96 \times$ standard deviation, on the left and to the absolute error between the NN mean prediction and the FE results on the right. In figures (a) and (b) we can see cases with high error in the maximum values that is outside the 95% CIs while in figures (c) and (d) there is high error in the maximum values but this error is contained inside the 95% CIs. Lastly in figures (e) and (f) we can see that the maximum values are predicted with high accuracy by the BNN and the error that exists in other areas is captured by the uncertainty of the BNN.

6 Conclusions

The goal of this work was to develop a CNN-based methodology to predict the effect of microscale features on the global stress field. We aimed for a Bayesian approach that would provide not a point estimation but Credible Intervals (CIs) for the prediction. We successfully managed to train a deterministic CNN on a simple dataset achieving 96% validation accuracy using 28,000 data points. We proceeded to a more advanced dataset with more interesting interactions and found that training using 23,000 data points only resulted in a 72% accuracy. We used rotation as a data augmentation technique in order to acquire more data with a minimum computational cost. With this approach by only using 5,000 data points, and applying 12 rotations, we were able to achieve an accuracy of 82%. Finally, we deployed a Bayesian Neural Network, able to provide uncertainty information for the predictions. The mean prediction of this network was able to fit the data very nicely, achieving a 72% validation accuracy using again 5,000 data points. The true result was inside the 95% CIs for 92% of the data points and also the uncertainty was higher close to the high error pixels. This suggests that the BNN is able to efficiently quantify the uncertainty of the prediction and provide high quality uncertainty that can be used in a Selective Learning framework. We demonstrated twice the advantages of the Selective Learning framework by comparing a random acquisition function with a maximum uncertainty acquisition function and showing that the latter results in a 40% reduction in the labeled data requirement. Also we examined the effect of the query rate on the efficiency of the Selective Learning process and concluded that too small or too large query rates should be avoided. Furthermore, we used Selective Learning to train the BNN with all the available data and we reached an accuracy of 84% by using 50% less data. Lastly, we tested the limits of our BNN by making predictions on points outside the training data distribution. The accuracy of course dropped but the important conclusion is that the network was able to efficiently quantify the uncertainty on the unseen cases. The real value was inside the prediction's 95% CIs for 80% of the cases.

Acknowledgments



This project has received funding from the European Union’s Horizon 2020 research and innovation programme under the Marie Skłodowska-Curie grant agreement No. 764644.

This paper only contains the author’s views and the Research Executive Agency and the Commission are not responsible for any use that may be made of the information it contains.

S.P.A. BORDAS thanks for the support of the Fonds National de la Recherche Luxembourg FNR grant O17-QCCAAS-11758809.

S.P.A. BORDAS received funding from the European Union’s Horizon 2020 research and innovation programme under grant agreement No 811099 TWINNING Project DRIVEN for the University of Luxembourg.

References

- Aladem, M. and Rawashdeh, S. A. (2020). A single-stream segmentation and depth prediction cnn for autonomous driving. *IEEE Intelligent Systems*, pages 1–1.
- Bishop, C. M. (1995). *Neural Networks for Pattern Recognition*. Oxford University Press, Inc., USA.
- Blundell, C., Cornebise, J., Kavukcuoglu, K., and Wierstra, D. (2015). Weight uncertainty in neural networks. arXiv: 1505.05424.
- Cheng, X., Li, X., Yang, J., and Tai, Y. (2018). Sesr: Single image super resolution with recursive squeeze and excitation networks. In *2018 24th International Conference on Pattern Recognition (ICPR)*, pages 147–152.
- Gal, Y. and Ghahramani, Z. (2016). Dropout as a bayesian approximation: Representing model uncertainty in deep learning. arXiv: 1506.02142.
- Gal, Y., Islam, R., and Ghahramani, Z. (2017). Deep bayesian active learning with image data. arXiv: 1703.02910.
- Garbin, C., Zhu, X., and Marques, O. (2020). Dropout vs. batch normalization: an empirical study of their impact to deep learning. *Multimedia Tools and Applications*, 79:1–39.
- Graves, A. (2011). Practical variational inference for neural networks. In Shawe-Taylor, J., Zemel, R. S., Bartlett, P. L., Pereira, F., and Weinberger, K. Q., editors, *Advances in Neural Information Processing Systems 24*, pages 2348–2356. Curran Associates, Inc.
- He, K., Zhang, X., Ren, S., and Sun, J. (2015). Deep residual learning for image recognition. arXiv: 1512.03385.
- Hinton, G. E. and van Camp, D. (1993). Keeping neural networks simple by minimizing the description length of the weights. In *Proceedings of the 16th Annual Conference On Learning Theory (COLT)*.

- Hochreiter, S., Bengio, Y., and Frasconi, P. (2001). Gradient flow in recurrent nets: the difficulty of learning long-term dependencies. In Kolen, J. and Kremer, S., editors, *Field Guide to Dynamical Recurrent Networks*. IEEE Press.
- Holub, A., Perona, P., and Burl, M. C. (2008). Entropy-based active learning for object recognition. In *CVPR Workshops*, pages 1–8.
- Hu, J., Shen, L., Albanie, S., Sun, G., and Wu, E. (2019). Squeeze-and-excitation networks. arXiv: 1709.01507.
- Ioffe, S. and Szegedy, C. (2015). Batch normalization: Accelerating deep network training by reducing internal covariate shift. arXiv: 1502.03167.
- Islam, R. (2016). Active learning for high dimensional inputs using bayesian convolutional neural networks.
- Jiang, H., Nie, Z., Yeo, R., Farimani, A. B., and Kara, L. B. (2020). Stressgan: A generative deep learning model for 2d stress distribution prediction. arXiv: 2006.11376.
- Joshi, A., Porikli, F., and Papanikolopoulos, N. (2009). Multi-class active learning for image classification. In *2009 IEEE Computer Society Conference on Computer Vision and Pattern Recognition Workshops, CVPR Workshops 2009, 2009 IEEE Computer Society Conference on Computer Vision and Pattern Recognition Workshops, CVPR Workshops 2009*, pages 2372–2379. IEEE Computer Society. 2009 IEEE Computer Society Conference on Computer Vision and Pattern Recognition ; Conference date: 20-06-2009 Through 25-06-2009.
- Kim, J., Lee, J. K., and Lee, K. M. (2016). Deeply-recursive convolutional network for image super-resolution. arXiv: 1511.04491.
- Kingma, D. P. and Welling, M. (2014). Auto-encoding variational bayes. arXiv: 1312.6114.
- Li, X., Chen, S., Hu, X., and Yang, J. (2018a). Understanding the disharmony between dropout and batch normalization by variance shift. arXiv: 1801.05134.
- Li, X. and Guo, Y. (2013). Adaptive active learning for image classification. In *Proceedings of the 2013 IEEE Conference on Computer Vision and Pattern Recognition, CVPR '13*, page 859–866, USA. IEEE Computer Society.
- Li, X., Wu, J., Lin, Z., Liu, H., and Zha, H. (2018b). Recurrent squeeze-and-excitation context aggregation net for single image deraining. In *Proceedings of the European Conference on Computer Vision (ECCV)*.
- Liang, L., Minliang, L., Caitlin, M., and Wei, S. (2018). A deep learning approach to estimate stress distribution: a fast and accurate surrogate of finite-element analysis. *Journal of the Royal Society, Interface*, 15:138.
- Lim, B., Son, S., Kim, H., Nah, S., and Lee, K. M. (2017). Enhanced deep residual networks for single image super-resolution. arXiv: 1707.02921.
- Meister, F., Passerini, T., Mihalef, V., Tuysuzoglu, A., Maier, A., and Mansi, T. (2018). Towards fast biomechanical modeling of soft tissue using neural networks. arXiv: 1812.06186.
- Mendizabal, A., Márquez-Neila, P., and Cotin, S. (2019). Simulation of hyperelastic materials in real-time using deep learning. *CoRR*, abs/1904.06197. arXiv: 1904.06197.
- Nie, Z., Jiang, H., and Kara, L. B. (2019). Stress field prediction in cantilevered structures using convolutional neural networks. *Journal of Computing and Information Science in Engineering*, 20(1).

- Pilkey, W. and Pilkey, D. (2008). Peterson’s stress concentration factors, third edition. *Peterson’s Stress Concentration Factors, Third Edition*, pages 1–522.
- Roewer-Despres, F., Khan, N., and Stavness, I. (2018). Towards finite-element simulation using deep learning.
- Sanchez-Palencia, E. (1986). Homogenization in mechanics, a survey of solved and open problems. *Rendiconti del Seminario Matematico*, 44(1):1–45.
- Santurkar, S., Tsipras, D., Ilyas, A., and Madry, A. (2019). How does batch normalization help optimization? arXiv: 1805.11604.
- Sasaki, H. and Igarashi, H. (2019). Topology optimization accelerated by deep learning. *IEEE Transactions on Magnetics*, 55(6):1–5.
- Sun, Y., Hanhan, I., Sangid, M. D., and Lin, G. (2020). Predicting mechanical properties from microstructure images in fiber-reinforced polymers using convolutional neural networks. arXiv: 2010.03675.
- Sussillo, D. and Abbott, L. F. (2015). Random walk initialization for training very deep feedforward networks. arXiv: 1412.6558.
- Tsybalov, E., Panov, M., and Shapeev, A. (2018). Dropout-based active learning for regression. *Analysis of Images, Social Networks and Texts*, page 247–258.
- Wang, Y., Oyen, D., Weihong, Guo, Mehta, A., Scott, C. B., Panda, N., Fernández-Godino, M. G., Srinivasan, G., and Yue, X. (2020). Stressnet: Deep learning to predict stress with fracture propagation in brittle materials.
- Wu, J., Yu, Y., Huang, C., and Yu, K. (2015). Deep multiple instance learning for image classification and auto-annotation. In *Proceedings of the IEEE Conference on Computer Vision and Pattern Recognition (CVPR)*.
- Zagoruyko, S. and Komodakis, N. (2017). Wide residual networks. arXiv: 1605.07146.
- Zhang, M., Li, W., and Du, Q. (2018). Diverse region-based cnn for hyperspectral image classification. *IEEE Transactions on Image Processing*, 27(6):2623–2634.
- Zhang, Y., Peng, B., Zhou, X., Xiang, C., and Wang, D. (2020). A deep convolutional neural network for topology optimization with strong generalization ability. arXiv: 1901.07761.